

# SCIENTIFIC REPORTS



OPEN

## Spine-to-Dendrite Calcium Modeling Discloses Relevance for Precise Positioning of Ryanodine Receptor-Containing Spine Endoplasmic Reticulum

Markus Breit<sup>1</sup>, Marcus Kessler<sup>1</sup>, Martin Stepniewski<sup>1</sup>, Andreas Vlachos<sup>2,3</sup> & Gillian Queisser<sup>4</sup> 

The endoplasmic reticulum (ER) forms a complex endomembrane network that reaches into the cellular compartments of a neuron, including dendritic spines. Recent work discloses that the spine ER is a dynamic structure that enters and leaves spines. While evidence exists that ER  $\text{Ca}^{2+}$  release is involved in synaptic plasticity, the role of spine ER morphology remains unknown. Combining a new 3D spine generator with 3D  $\text{Ca}^{2+}$  modeling, we addressed the relevance of ER positioning on spine-to-dendrite  $\text{Ca}^{2+}$  signaling. Our simulations, which account for  $\text{Ca}^{2+}$  exchange on the plasma membrane and ER, show that spine ER needs to be present in distinct morphological conformations in order to overcome a barrier between the spine and dendritic shaft. We demonstrate that RyR-carrying spine ER promotes spine-to-dendrite  $\text{Ca}^{2+}$  signals in a position-dependent manner. Our simulations indicate that RyR-carrying ER can initiate time-delayed  $\text{Ca}^{2+}$  reverberation, depending on the precise position of the spine ER. Upon spine growth, structural reorganization of the ER restores spine-to-dendrite  $\text{Ca}^{2+}$  communication, while maintaining aspects of  $\text{Ca}^{2+}$  homeostasis in the spine head. Our work emphasizes the relevance of precise positioning of RyR-containing spine ER in regulating the strength and timing of spine  $\text{Ca}^{2+}$  signaling, which could play an important role in tuning spine-to-dendrite  $\text{Ca}^{2+}$  communication and homeostasis.

The endoplasmic reticulum (ER) is a multifunctional intracellular organelle, which consists of a complex three-dimensional network of connected endomembrane tubules, stacks and cisternae<sup>1-4</sup>. In neurons, the relevance of its strategic positioning is reflected by the fact that it reaches from the nucleus and soma into neurites, i.e., dendrites and axons, and it is frequently found in proximity of excitatory and inhibitory pre- and postsynaptic sides. This observation has coined the term “neuron within a neuron” for neuronal ER morphology<sup>5</sup>. While its role in synaptic protein synthesis, protein maturation, and transport is still debated, it is best-studied for its ability to release  $\text{Ca}^{2+}$  in a receptor-dependent manner, which modulates the capacity of synapses to undergo plastic changes<sup>2,6-9</sup>.

The ER consists of a complex, overlapping and partially cell- and region-specific  $\text{Ca}^{2+}$  handling machinery, including  $\text{Ca}^{2+}$  pumps and transporters<sup>2</sup>. In hippocampal neurons, for example, inositol trisphosphate receptors ( $\text{IP}_3\text{R}$ ) are present at high concentrations in dendritic shafts and cell bodies, whereas ryanodine receptors (RyR) are primarily found in dendritic spines and axons<sup>10</sup> (see also<sup>11</sup>). In contrast, Purkinje cells of the cerebellum show high concentrations of  $\text{IP}_3\text{R}$  also in dendritic spines<sup>12,13</sup>. Whether these receptors are evenly distributed along the spine ER compartment or rather clustered at strategic positions remains unknown. More recent work has also established a link between store-operated  $\text{Ca}^{2+}$  entry (SOCE), i.e., ORAI-STIM1-mediated  $\text{Ca}^{2+}$  signaling, and neuronal ER-mediated plasticity (e.g.<sup>14,15</sup>). Another major challenge in this field of research is the fact that the

<sup>1</sup>Goethe Center for Scientific Computing, Computational Neuroscience, Goethe University Frankfurt, Frankfurt, Germany. <sup>2</sup>Department of Neuroanatomy, Institute of Anatomy and Cell Biology, Faculty of Medicine, University of Freiburg, Freiburg, 79104, Germany. <sup>3</sup>Bernstein Center Freiburg, University of Freiburg, Freiburg, 79104, Germany. <sup>4</sup>Department of Mathematics, Temple University, Philadelphia, USA. Markus Breit and Marcus Kessler contributed equally. Andreas Vlachos and Gillian Queisser jointly supervised this work. Correspondence and requests for materials should be addressed to A.V. (email: [andreas.vlachos@anat.uni-freiburg.de](mailto:andreas.vlachos@anat.uni-freiburg.de)) or G.Q. (email: [gillian.queisser@temple.edu](mailto:gillian.queisser@temple.edu))

ER is a dynamic structure that can rapidly enter and leave pre-existing spines, while changing its position within individual ER-positive spines<sup>16,17</sup>. Hence, it is conceivable that spine-to-dendrite  $\text{Ca}^{2+}$  communication may critically depend on (1) whether or not a spine contains ER, (2) ER  $\text{Ca}^{2+}$  receptor composition, and (3) the precise ER morphology and position within a spine.

In order to capture how distinct spine ER properties influence spine-to-dendrite  $\text{Ca}^{2+}$  communication, the three-dimensional intracellular architecture must be considered<sup>18,19</sup>. Therefore, we developed a new spine and ER generator for the simulation framework NeuroBox<sup>20</sup> to parametrically design three-dimensional computational domains (Fig. 1a). Existing single-channel models of  $\text{Na}^+/\text{Ca}^{2+}$  exchangers in the plasma membrane, as well as RyR, IP<sub>3</sub>R and sarco/endoplasmic reticulum  $\text{Ca}^{2+}$  ATPases (SERCA) on the ER membrane (see schematic in Fig. 1c) were adapted and integrated in a novel three-dimensional calcium model that is solved by established numerical methods (details provided in Methods). Using this novel framework, we systematically assessed the relevance of selected spine ER properties, i.e., length, width and presence of RyR and IP<sub>3</sub>R on spine-to-dendrite  $\text{Ca}^{2+}$  signaling.

## Results

**Passive spine ER has no major impact on spine-to-dendrite  $\text{Ca}^{2+}$  signaling.** To assess the role of spine ER positioning in spine-to-dendrite  $\text{Ca}^{2+}$  communication, we first investigated  $\text{Ca}^{2+}$  signal propagation in a representative 3D spine model not containing any ER. The simplified morphology of the spine (Fig. 1a) is based on mean values obtained from stimulated emission depletion (STED) live cell microscopy experiments<sup>21</sup>.  $\text{Ca}^{2+}$  ions were released into the spine head with three distinct release profiles, i.e., a 1 ms release and two longer release periods with a 10 ms and 150 ms time constant, respectively. Changes in  $[\text{Ca}^{2+}]$  were determined in the indicated regions of interest (Fig. 1b), i.e., in the spine head, neck and dendrite.

As shown in Fig. 2 for 1 ms initial  $\text{Ca}^{2+}$  release, only a small fraction of  $\text{Ca}^{2+}$  reaches the dendritic compartment ( $<1\%$ ; Fig. 2b). When the spine ER is passive, i.e., when it is present as a geometric obstacle, but without any  $\text{Ca}^{2+}$  exchange mechanisms that would allow  $\text{Ca}^{2+}$  exchange across the ER membrane, nearly identical and near-zero dendritic  $\text{Ca}^{2+}$  profiles for all ER lengths are observed (Fig. 2b)<sup>22</sup>. Similar results were obtained for the longer  $\text{Ca}^{2+}$  influx durations (c.f., Supplemental Fig. S1). From these results we conclude that spine-to-dendrite  $\text{Ca}^{2+}$  signaling is negligible in the no-spine-ER and the passive-spine-ER setting. Accordingly, precise positioning of a purely passive spine ER compartment has only minor effects on spine-to-dendrite  $\text{Ca}^{2+}$  signals in our experimental setting. This observation strengthens the case for active  $\text{Ca}^{2+}$  exchange across the spine ER membrane to enable spine-to-dendrite  $\text{Ca}^{2+}$  communication.

**Ryanodine receptor-containing ER promotes spine-to-dendrite  $\text{Ca}^{2+}$  signaling.** We next tested for the role of RyR-containing ER introduced to the spine compartment. Indeed, RyR promoted and even amplified spine-to-dendrite  $\text{Ca}^{2+}$  signals in our experimental setting (1 ms initial  $\text{Ca}^{2+}$  release illustrated in Fig. 3): For an ER length of 1.5  $\mu\text{m}$  (width 0.036  $\mu\text{m}$ ; cf. Fig. 3a and Table 1), an approximately 20fold increase in  $[\text{Ca}^{2+}]$  was measured in the spine neck (as compared to the purely passive spine ER setting), while up to twice the amount of  $\text{Ca}^{2+}$  initially released into the spine head was observed in the dendrite (Fig. 3b; see also supplemental movie). In addition, an increase in spine head  $[\text{Ca}^{2+}]$  was observed as soon as the ER reached the border between the spine neck and head, while  $[\text{Ca}^{2+}]$  in the neck and dendrite was comparable under these conditions. RyR-ER at the base of the spine (ER length 0.5  $\mu\text{m}$ ) had no apparent effect on spine-to-dendrite  $\text{Ca}^{2+}$  communication (Fig. 3b). These simulations indicate that the precise position of RyR-containing ER could have an impact on spine-to-dendrite  $\text{Ca}^{2+}$  signaling and  $\text{Ca}^{2+}$  signal amplification.

**IP<sub>3</sub> receptors introduce protracted  $\text{Ca}^{2+}$  waves in the spine head and neck.** While it has been argued that spine ER may not contain IP<sub>3</sub>Rs in hippocampal neurons<sup>10</sup>, our computational approach enabled us to evaluate the behavior of IP<sub>3</sub>R-only spine ER. Fig. 3c shows a slow rise in  $[\text{Ca}^{2+}]$  in the head and neck of spines in response to 1 ms  $\text{Ca}^{2+}$  influx and simultaneous onset of a 200 ms IP<sub>3</sub> release, which became more prominent as the ER reached the spine head. In our simulations, IP<sub>3</sub>R-only spine ER, similar to a passive ER, does not have the ability to initiate strong spine-to-dendrite communication. Interestingly, although much weaker as compared to RyR-containing ER (cf. Fig. 3b), a small  $\text{Ca}^{2+}$  increase was even observed with ER of length 0.5  $\mu\text{m}$ . We attribute this difference between RyR- and IP<sub>3</sub>R-containing ER to (1) the presence of  $\text{Ca}^{2+}$  buffers, which scavenge  $\text{Ca}^{2+}$  and limit its reach, while IP<sub>3</sub> has a slower decay rate compared to  $\text{Ca}^{2+}$ , and therefore a longer reach toward the dendrite, and (2) the fact that IP<sub>3</sub>R is activated at lower  $[\text{Ca}^{2+}]$  in the presence of IP<sub>3</sub>. Thus, IP<sub>3</sub>R-mediated  $\text{Ca}^{2+}$  signals are weaker than RyR- $\text{Ca}^{2+}$  signals, but are sensitive to low  $[\text{Ca}^{2+}]$  even at spine ER positions distant from the synapse.

**Combining RyR and IP<sub>3</sub>R can cause delayed  $\text{Ca}^{2+}$  signal reverberation.** Based on the results above, we speculated that the slow protracted IP<sub>3</sub>R-mediated  $\text{Ca}^{2+}$  -response could trigger RyR-mediated  $\text{Ca}^{2+}$  release from the ER in situations where RyR-only ER is not sufficient to promote spine-to-synapse communication. Thus, IP<sub>3</sub>R-mediated  $\text{Ca}^{2+}$  responses could support RyR-mediated  $\text{Ca}^{2+}$  signaling between spines and dendrites.

To test this hypothesis, we repeated our simulations with spine ER containing both RyR and IP<sub>3</sub>R. ER positions in the neck and head of the spine elicited  $\text{Ca}^{2+}$  dynamics that were comparable to the RyR-only simulations (Fig. 3d). When, however, the RyR/IP<sub>3</sub>R-containing ER was positioned at the base of the spine, an additional protracted  $\text{Ca}^{2+}$  response was observed, which propagated back toward the spine head compartment, but dissipated along the way due to  $\text{Ca}^{2+}$  buffering. This result is in line with the literature disclosing ER-mediated IP<sub>3</sub>-dependent protracted  $\text{Ca}^{2+}$  signals, which may promote long-term depression of excitatory neurotransmission, e.g.<sup>11,23,24</sup>.

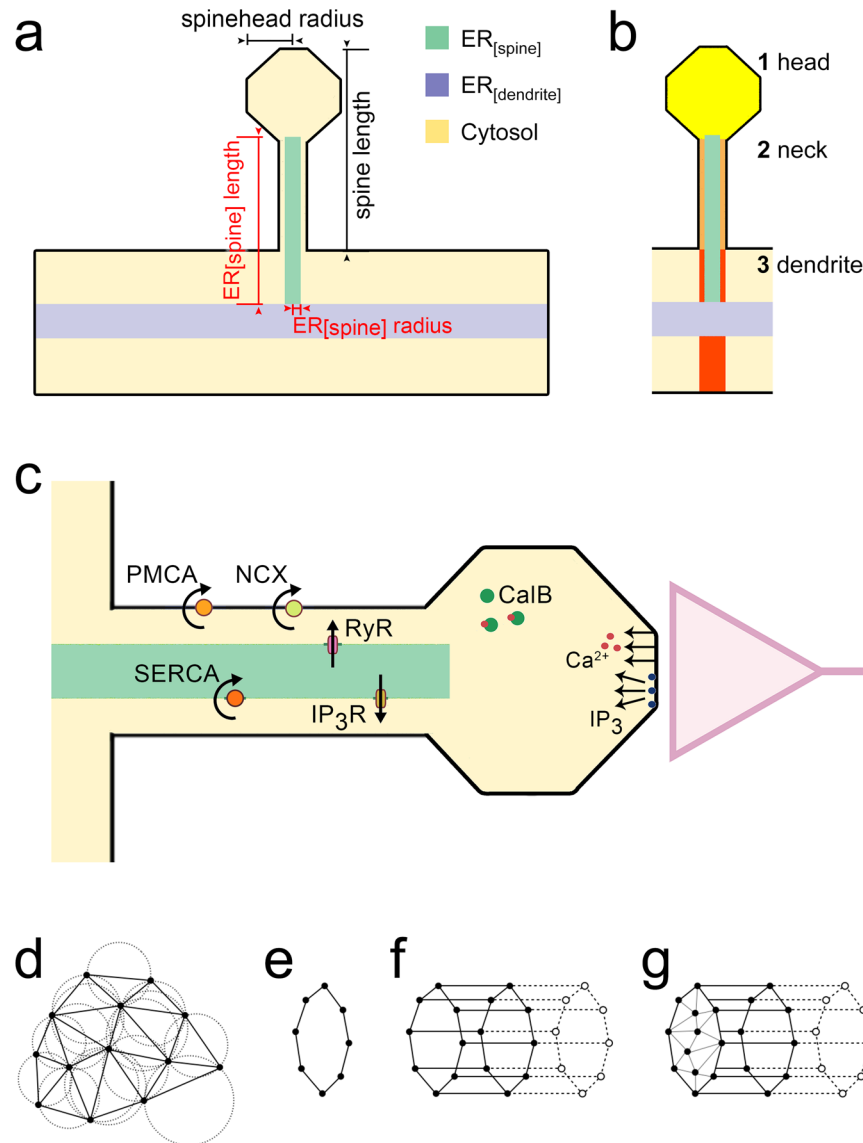


**Figure 1.** Spine  $\text{Ca}^{2+}$  modeling. (a) Schematic illustration of a single spine emerging from a dendrite containing endoplasmic reticulum (ER). Spine ER ( $\text{ER}_{[\text{spine}]}$ , green) reaches into the spine compartment. The relevant parameters evaluated in this study are indicated. Spine morphology is based on average values of  $f^{21}$ , who used stimulated emission depletion (STED) microscopy to determine parameters such as spine length, spine head size and spine neck width. (b,c) Upon release of  $\text{Ca}^{2+}$  ions and inositol trisphosphate ( $\text{IP}_3$ ) molecules in the head of the spine, changes in  $[\text{Ca}^{2+}]$  are determined in the head (yellow), neck (orange) and dendritic region (red), respectively. The model accounts for  $\text{Ca}^{2+}$  exchange mechanisms on the plasma membrane ( $\text{Na}^+/\text{Ca}^{2+}$  exchangers (NCX), plasma membrane  $\text{Ca}^{2+}$  -ATPases (PMCA)) and on the ER (inositol trisphosphate receptors ( $\text{IP}_3\text{R}$ ), ryanodine receptors (RyR), and sarco/endoplasmic reticulum  $\text{Ca}^{2+}$  -ATPases (SERCA)). (d) Sample 2D triangulation  $\mathcal{S} = \{T_1, \dots, T_M\}$  with fulfilled Delaunay condition, i.e., the unique circumcircle of each  $T_i$ , which passes through the three triangular vertices, does not contain any vertices of the grid in its interior. (e) Piecewise linear approximation of a circle with 8 rim vertices as used for the construction of the dendrite, ER and spine structures in the spine generator. (f) Successive circle extrusion with creation of quadrilateral faces enclosing the emerging cylinder barrel during dendrite, ER and spine structure generation. (g) Exemplary triangulation of the planar hole at the left cylinder side as used for closing the encapsulated spine surface geometry. Further details are provided in Tables 1 and 2. See also supplemental movie.

**The precise position of RyR-containing ER may affect the timing of  $\text{Ca}^{2+}$  signals.** Motivated by the observation that ER positioning affects  $\text{Ca}^{2+}$  signals, we next determined the position of RyR spine ER at which spine-to-dendrite communication and  $\text{Ca}^{2+}$  signal amplification occurs. Figure 4 shows the transition that occurs for a 1 ms  $\text{Ca}^{2+}$  influx when growing the ER beyond a critical length. While no  $\text{Ca}^{2+}$  signal can be detected in the dendrite for an ER length of  $0.75\ \mu\text{m}$  in the RyR-only case (Fig. 4a,b), spine-to-dendrite communication is detectable for a length of  $0.8\ \mu\text{m}$  (Fig. 4a,c). While the exact position of this transition zone depends on the

Parameter name	Description	Value (range) [ $\mu\text{m}$ ]
dendrite radius	radius of dendrite segment	0.45
dendrite length	length of dendrite segment	10.0
spine neck radius	radius of spine neck	0.08
spine neck length	length of spine neck	0.7
spine head radius	radius of spine head	0.29
dendrite ER radius	radius of dendritic ER	0.11
dendrite ER length	length of dendritic ER	8.0
spine ER radius	radius of spine neck ER	0.036–0.054
spine ER length	length of spine neck ER	0–1.7
spine ER head radius	radius of spine ER head	0–0.12

**Table 1.** Geometrical parameters of the spine model. All length parameters are given in units of  $\mu\text{m}$ .

Initial and equilibrium values			SERCA pumps		
$c_c$	50 nM	(chosen)	$I_S$	$6.5 \times 10^{-21} \text{ mol} \mu\text{m} \text{ s}^{-1}$	<sup>99</sup> (adapt.)
$c_e$	250 $\mu\text{M}$	(chosen)	$K_S$	180 nM	<sup>86</sup>
$c_o$	2 mM	(chosen)	$\rho_S$	$2390 \mu\text{m}^{-2}$	<sup>98</sup> (approx.)
$p$	40 nM	<sup>95</sup>	<b>PMCA pumps</b>		
$b^{\text{tot}}$	40 $\mu\text{M}$	<sup>96</sup>	$I_P$	$1.7 \times 10^{-23} \text{ mol s}^{-1}$	<sup>87</sup>
<b>Diffusion/reaction</b>			$K_P$	60 nM	<sup>100</sup>
$D_c$	$220 \mu\text{m}^2 \text{ s}^{-1}$	<sup>77</sup>	$\rho_P$	$500 \mu\text{m}^{-2}$	(estim.)
$D_p$	$280 \mu\text{m}^2 \text{ s}^{-1}$	<sup>77</sup>	<b>NCX pumps</b>		
$D_b$	$20 \mu\text{m}^2 \text{ s}^{-1}$	<sup>78</sup>	$I_N$	$2.5 \times 10^{-21} \text{ mol s}^{-1}$	<sup>87</sup> (adapt.)
$\kappa_b^-$	$19 \text{ s}^{-1}$	<sup>96</sup>	$K_N$	1.8 $\mu\text{M}$	<sup>87</sup>
$\kappa_b^+$	$27 \mu\text{M}^{-1} \text{ s}^{-1}$	<sup>96</sup>	$\rho_N$	$15 \mu\text{m}^{-2}$	(estim.)
$\kappa_p$	$0.11 \text{ s}^{-1}$	<sup>97</sup>			
$p^r$	40 nM	<sup>95</sup>	<b>leakage</b>		
<b>IP<sub>3</sub>R channel</b>			$v_{l,e}$	38 $\text{nms}^{-1}$	(calc.)
$d_1$	0.13 $\mu\text{M}$	<sup>83</sup>	$v_{l,p}$	4.5 $\text{nms}^{-1}$	(calc.)
$d_2$	1.05 $\mu\text{M}$	<sup>83</sup>	<b>calcium/IP<sub>3</sub> release</b>		
$d_3$	0.94 $\mu\text{M}$	<sup>83</sup>	$j_c^{\text{rls}}$	$1.0 \times 10^{-16} \text{ mol s}^{-1} \mu\text{m}^{-2}$	1 ms release
$d_5$	82.3 nM	<sup>83</sup>		$5.0 \times 10^{-17} \text{ mol s}^{-1} \mu\text{m}^{-2}$	10 ms release
$\rho_I$	$17.3 \mu\text{m}^{-2}$	<sup>98</sup>	$\tau_{\text{rls}}$	10 ms	
$I_I^{\text{ref}}$	$1.1 \times 10^{-19} \text{ mol s}^{-1}$	<sup>82</sup> (extrapol.)	$\tau_{\text{NMDAR}}$	150 ms	
<b>RyR channel</b>			$\rho_{\text{NMDAR}}$	$8.15 \times 10^{-3} \mu\text{m}^3 \text{ s}^{-1}$	
$k_a^-$	$28.8 \text{ s}^{-1}$	<sup>84</sup>	$\hat{V}$	13.4 mV	
$k_a^+$	$1500 \mu\text{M}^{-4} \text{ s}^{-1}$	<sup>84</sup>	$j_p^{\text{rls}}$	$5.0 \times 10^{-18} \text{ mol s}^{-1} \mu\text{m}^{-2}$	<sup>92</sup> (adapt.)
$k_b^-$	$385.9 \text{ s}^{-1}$	<sup>84</sup>			
$k_b^+$	$1500 \mu\text{M}^{-3} \text{ s}^{-1}$	<sup>84</sup>			
$k_c^-$	$0.1 \text{ s}^{-1}$	<sup>84</sup>			
$k_c^+$	$1.75 \text{ s}^{-1}$	<sup>84</sup>			
$\rho_R$	$3.0 \mu\text{m}^{-2}$	(estim.)			
$I_R^{\text{ref}}$	$3.5 \times 10^{-18} \text{ mol s}^{-1}$	<sup>85</sup> (approx.)			

**Table 2.** Model parameters and initial values.

initial  $\text{Ca}^{2+}$  release in the spine head (i.e., total number of  $\text{Ca}^{2+}$  ions and release current density), the effects of the spine ER within this critical zone are robust. In case of a prolonged, i.e., 150 ms  $\text{Ca}^{2+}$  influx, the transition is found between ER lengths of 0.4  $\mu\text{m}$  and 0.45  $\mu\text{m}$  (c.f., Supplemental Fig. S2). Interestingly, a delay in the  $\text{Ca}^{2+}$  signal occurs at these transition positions, which can be attributed to the fact that it takes several milliseconds at this transition length for  $\text{Ca}^{2+}$  to reach the critical threshold that triggers RyR-mediated  $\text{Ca}^{2+}$  release from the ER.

Consistent with the results described above, IP<sub>3</sub>R- and RyR-containing ER at a position, which does not elicit RyR-only responses, triggered the described delayed IP<sub>3</sub>R-mediated RyR-dependent  $\text{Ca}^{2+}$  response (Fig. 4d). These findings suggest that the precise position of RyR-(IP<sub>3</sub>R)-containing ER (1) enables spine-to-dendrite  $\text{Ca}^{2+}$  signaling, (2) amplifies the  $\text{Ca}^{2+}$  signal, and may even (3) modulate the exact timing of the  $\text{Ca}^{2+}$  signal. Considering that the outcome of plasticity may critically depend on such timing<sup>25–27</sup>, i.e., coincidence detection, this appears to be a relevant observation.

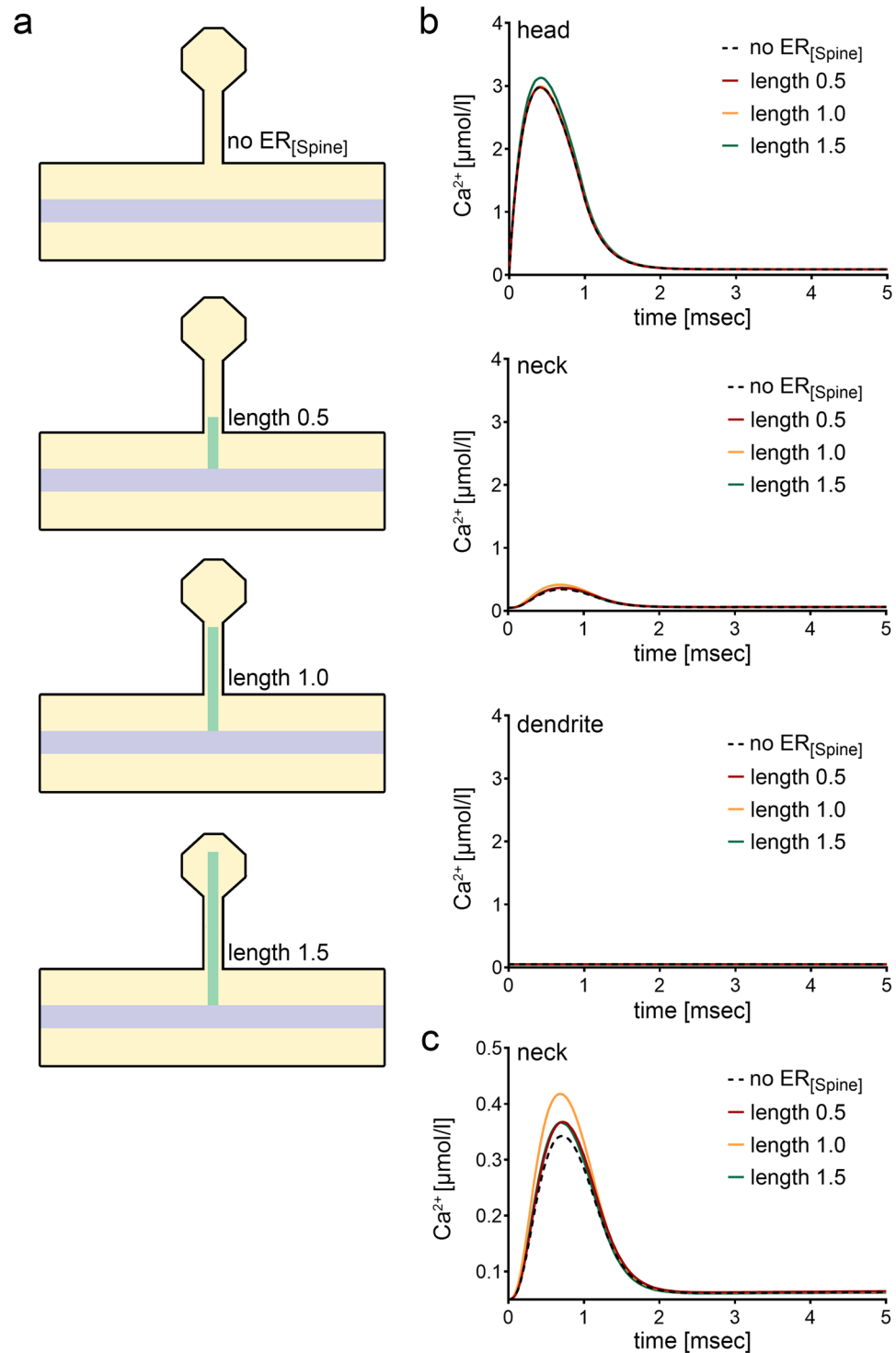


**Figure 2.** Effects of passive spine ER on spine-to-dendrite Ca<sup>2+</sup> signaling. **(a)** Schematics of three selected morphological settings. Spine ER length is given in units of  $\mu\text{m}$ . **(b)** Ca<sup>2+</sup> profiles for 1 ms initial Ca<sup>2+</sup> release into the spine head (cf. Supplemental Fig. S1). Consistent with experimental data, spine-to-dendrite Ca<sup>2+</sup> signaling does not occur in our simulations. Presence or length of passive spine ER has only minor effects on Ca<sup>2+</sup> dynamics in the spine head and neck. Ca<sup>2+</sup> buffering has a major impact in these simulations, thus inactivating spine-to-dendrite Ca<sup>2+</sup> communication. **(c)** Minor effects of the passive spine ER on the Ca<sup>2+</sup> profile are shown at higher magnification for the spine neck.

### RyR-ER-dependent spine-to-dendrite Ca<sup>2+</sup> coupling does not depend on the length of the spine.

To test for the role of spine length, we carried out a series of simulations in which a very long spine, i.e.,  $10\mu\text{m}$  spine neck length, was used. All other spine parameters were kept constant. The following major conclusions

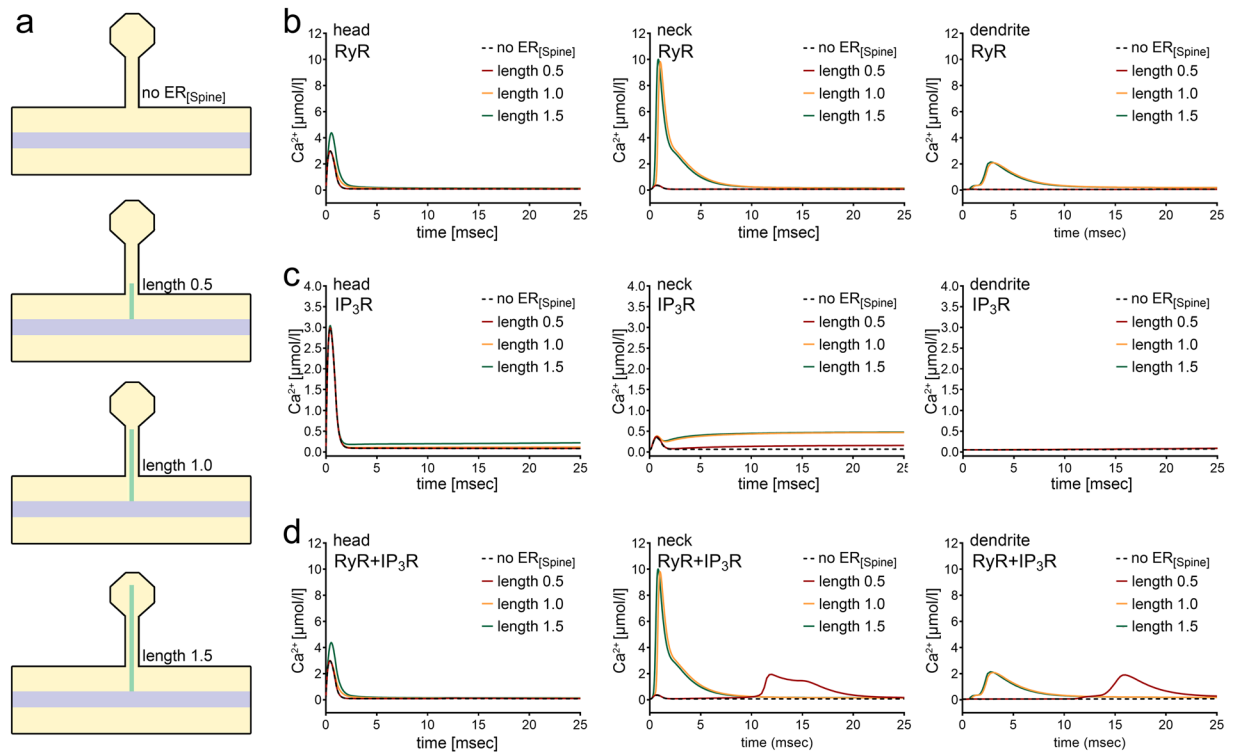


**Figure 3.** Differential effects of spine ER carrying ryanodine receptor (RyR) and inositol triphosphate receptor ( $\text{IP}_3\text{R}$ ) on spine-to-dendrite  $\text{Ca}^{2+}$  signaling. **(a)** Schematics of spine ER morphologies used to investigate the role of RyR- and  $\text{IP}_3\text{R}$ -mediated  $\text{Ca}^{2+}$  release. Spine ER width is kept constant, while the length is varied between 0–1.5  $\mu\text{m}$ . **(b)**  $\text{Ca}^{2+}$  profiles in response to 1 ms  $\text{Ca}^{2+}$  influx into the spine head for the four configurations depicted in **(a)** in the spine head, neck, and dendrite (from left to right) for RyR-only spine ER. **(c)**  $\text{Ca}^{2+}$  profiles for the four configurations depicted in **(a)** in the spine head, neck, and dendrite (from left to right) for  $\text{IP}_3\text{R}$ -only spine ER. Note that the plateau in the neck profile appears to be small compared to RyR-induced dynamics, as the plateau effect is overshadowed by the RyR dynamics in **(b)** and **(d)**. **(d)**  $\text{Ca}^{2+}$  profiles for the four configurations depicted in **(a)** for spine ER carrying both RyR and  $\text{IP}_3\text{R}$ .

were drawn from this series of simulations: (1) RyR-ER couples and amplifies  $\text{Ca}^{2+}$  signals in dendrites and very long spines, (2) RyR-dependent spine-to-dendrite  $\text{Ca}^{2+}$  signal coupling occurs once the ER reaches far enough into the spine (Fig. 5b, position 3), (3) spine ER reaching even further into the spine makes spine head  $\text{Ca}^{2+}$  levels increase, (4) at a position that does not show RyR-dependent  $\text{Ca}^{2+}$  release from intracellular stores, introducing  $\text{IP}_3\text{R}$  establishes a slightly delayed spine-to-dendrite communication (Fig. 5b,c, positions 1, 2). (5) Positioning RyR-only ER at the critical transition length – depending on the initial  $\text{Ca}^{2+}$  release in the spine head – has a similar “delaying” effect on  $\text{Ca}^{2+}$  signals (cf. Fig. 4).

**Role of spine RyR-ER in spine head  $\text{Ca}^{2+}$  homeostasis during plasticity.** Finally, we tested for the effects of an increase in spine head volume, as seen after the induction of synaptic plasticity (e.g.<sup>28–30</sup>). Considering unchanged  $\text{Ca}^{2+}$  entry, we wondered whether changes in ER morphology, i.e., ER position and size, compensate for changes in spine-to-dendrite  $\text{Ca}^{2+}$  signaling as the size of the spine head increases. As illustrated in the spine schematics (Fig. 6a), spine head volume was increased by a factor of 2. Depending on the position of the spine ER, this can lead to a loss of spine-to-dendrite communication as well as a considerable decrease in  $[\text{Ca}^{2+}]$  in the spine head (Fig. 6b,c).

Increasing the length of the ER (length 1.1  $\mu\text{m}$ ; width 0.036  $\mu\text{m}$ ) or changing the width of the ER (length 1.0  $\mu\text{m}$ ; width 0.054  $\mu\text{m}$ ) reactivated spine-to-dendrite communication upon an initial 1 ms  $\text{Ca}^{2+}$  release in the spine head (Fig. 6d). However, it is not possible to fully restore the original  $\text{Ca}^{2+}$  profile, even when the ER is grown all the way close to the  $\text{Ca}^{2+}$  entry site (length 1.7  $\mu\text{m}$ , width 0.036  $\mu\text{m}$ ; Fig. 6d).

Based on systematic evaluation, we finally determined that a selective volume increase in the ER segment located in the spine head (“spine-within-spine” morphology) leads to the best possible recovery of the  $\text{Ca}^{2+}$  profile in the spine head, neck and dendrite under conditions of increased spine head volume (Fig. 6e). For simulations with  $\text{Ca}^{2+}$  release of longer duration, the peak amplitude of the  $\text{Ca}^{2+}$  signal in the spine head is also restored with the “spine-within-spine” ER morphology. The decay dynamics in the head, however, become sharper in comparison (Fig. 6f). The reason lies in the limited ER  $\text{Ca}^{2+}$  store capacity, which rapidly depletes in our experimental setting. In the tested scenarios, dendritic dynamics were restored by morphological reorganization of the spine ER, which did not require a “spine-within-spine” morphology. Hence, complex changes in spine ER

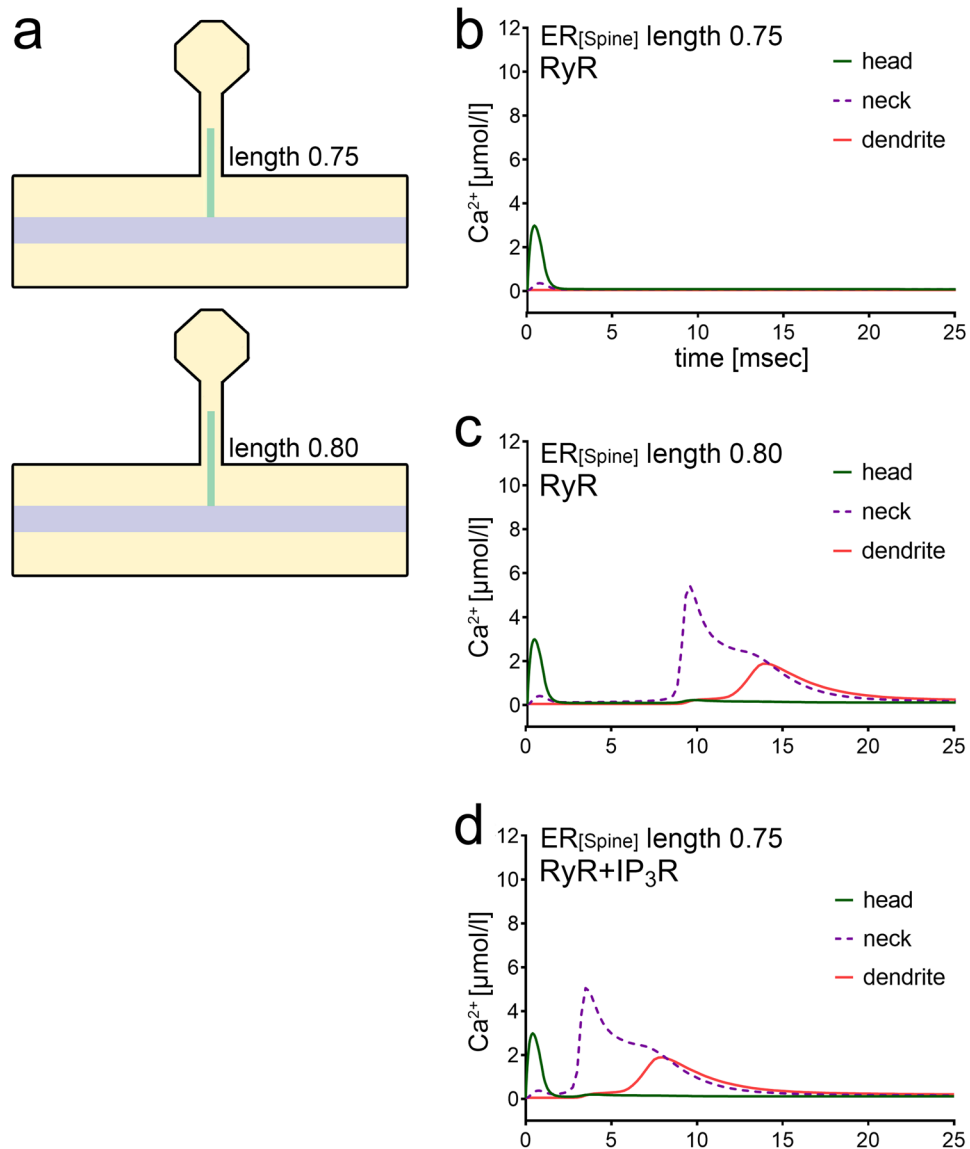


**Figure 4.** Critical spine ER transition lengths regulate all-or-nothing spine-to-dendrite communication. **(a)** Schematics of three morphological configurations designed to illustrate  $\text{Ca}^{2+}$  signals around critical ER transition lengths in response to 1 ms  $\text{Ca}^{2+}$  influx into the spine head. **(b)** For a RyR-containing ER of length  $0.75 \mu\text{m}$ , no  $\text{Ca}^{2+}$  communication to the dendrite is detected. **(c)** Increasing the RyR-containing ER to a length of  $0.8 \mu\text{m}$  surpasses a critical spine ER length to trigger spine-to-dendrite communication. At this critical length,  $[\text{Ca}^{2+}]$  in the vicinity of the ER membrane is elevated just above the CICR threshold. This occurs after the initial dampened and diluted (by diffusion)  $\text{Ca}^{2+}$  signal, visible in the first milliseconds, propagates to the ER membrane and eventually triggers delayed CICR at roughly 8 ms. In the roughly 5 ms period leading to store release, one can observe the slow elevation of local cytosolic  $\text{Ca}^{2+}$  concentration that eventually surpasses the threshold necessary to trigger self-reinforcing  $\text{Ca}^{2+}$  release from the ER. **(d)** Adding  $\text{IP}_3\text{R}$  to the ER allows for spine-to-dendrite signals at an ER length for which RyR-only ER is not capable of transmitting a signal to the dendrite (see panel (b) of this figure). The exact position of this transition zone depends on the initial  $\text{Ca}^{2+}$  release in the spine head (cf. Supplemental Fig. S2).

morphology seem to be required to restore  $\text{Ca}^{2+}$  homeostasis in the spine head, while precise positioning of the ER suffices to restore spine-to-dendrite  $\text{Ca}^{2+}$  communication.

### Discussion

The present study highlights how functional and structural spine ER properties may affect spine-to-dendrite  $\text{Ca}^{2+}$  signaling. While precise positioning of RyR-( $\text{IP}_3\text{R}$ )-containing spine ER has a major impact on spine-to-dendrite  $\text{Ca}^{2+}$  communication, affecting both the strength and timing of the signal, growth of the spine neck or the spine head can cause a disruption of  $\text{Ca}^{2+}$  signaling. Eventually, comparable  $\text{Ca}^{2+}$  profiles can be restored by changes in ER morphology, i.e., position and size. These restoration effects could be demonstrated for  $\text{Ca}^{2+}$  entry profiles

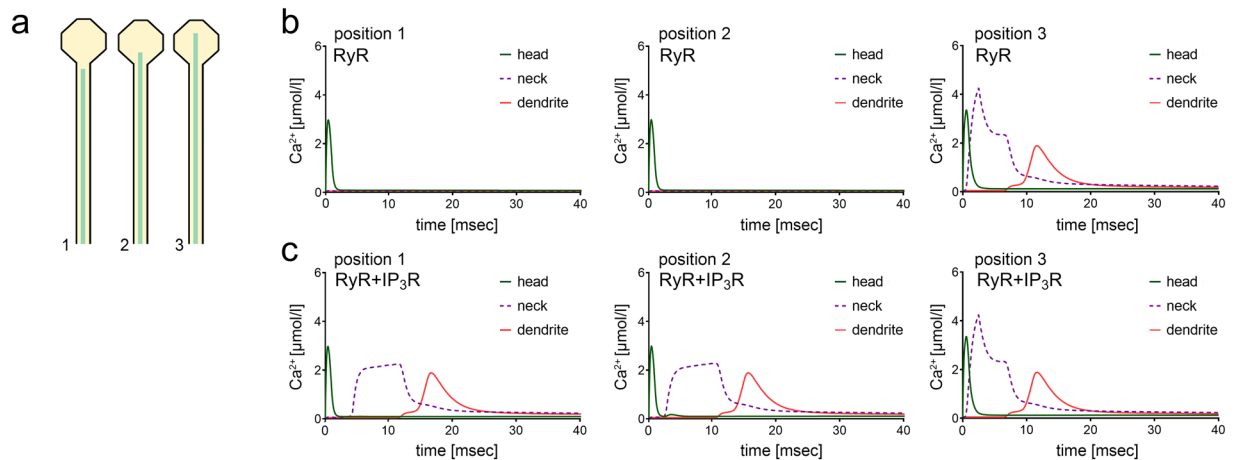


**Figure 5.** Precisely positioned active ER enables spine-to-dendrite  $\text{Ca}^{2+}$  communication in a very long spine. **(a)** Illustration of the three ER positions used for the simulations in **(b)** and **(c)**. A very long spine neck ( $10\ \mu\text{m}$ ) was employed to investigate whether neck length is a limiting factor for ER-mediated spine-to-dendrite  $\text{Ca}^{2+}$  communication. **(b)** Simulations for a RyR-only ER at positions 1, 2 and 3 in response to 1 ms  $\text{Ca}^{2+}$  influx into the spine head (illustrated in panel **(a)** of this figure). **(c)** Addition of  $\text{IP}_3\text{R}$  enables spine-to-dendrite  $\text{Ca}^{2+}$  communication at ER positions farther away from the synapse. Note the comparable  $\text{Ca}^{2+}$  profiles at position 3 between RyR-only and RyR+  $\text{IP}_3\text{R}$  ER.

with different strength/duration. The all-or-none transition points as shown in Figs 4 and 5 are detectable for all tested entry profiles, the transition points, however, shift closer towards or farther away from the spine head, depending on the  $\text{Ca}^{2+}$  entry profile. It appears that not the absolute length or volume of the spine neck and head, respectively, determine the nature of spine-to-dendrite  $\text{Ca}^{2+}$  communication, but rather the relationship between spine morphology and spine ER morphology (“spine-within-spine” morphology). The presence of RyR and  $\text{IP}_3\text{R}$  is important in this context. Once critical distances between the postsynaptic density and the ER are overcome and/or volume ratios between spine head and ER in the spine head are met, the synapse regains its previous spine-to-dendrite  $\text{Ca}^{2+}$  communication.

The role of spine ER in synaptic plasticity remains a matter of debate. For example, controversial results exist with respect to the relevance of ER  $\text{Ca}^{2+}$  stores in synaptic calcium transients<sup>11,28,31–35</sup>. This is in part explained by technical limitations in simultaneously visualizing (1) dendritic spine morphology, (2) presence and precise position of spine ER, and (3) in releasing reproducible amounts of  $\text{Ca}^{2+}$  while (4) carrying out  $\text{Ca}^{2+}$  imaging at high temporal and spatial resolution. Also, it is currently not possible to systematically assess the relevance of individual spine and ER parameters, as they are not easy to manipulate in biologically complex systems. We used a computational approach to compare ER-negative and ER-positive spines and to assess the role of spine ER morphology in spine  $\text{Ca}^{2+}$  transients. We show that critical ER lengths can be determined for specific spine geometries, functioning as a binary switch for spine-to-dendrite signaling. While the precise position depends on a given  $\text{Ca}^{2+}$  entry profile, beyond this all-or-nothing regulation, ER positioning can also function at the more refined level of timing. Our simulations suggest that the timing of a dendritic  $\text{Ca}^{2+}$  signal is determined by ER position and RyR/ $\text{IP}_3\text{R}$  configuration. In some cases, even signals reverberating in the spine neck can be detected. In addition, peak amplitudes of  $\text{Ca}^{2+}$  transients are affected. Considering the relevance of  $\text{Ca}^{2+}$  signaling in synaptic plasticity and coincidence detection, i.e., spike-timing-dependent plasticity<sup>25–27</sup>, our findings imply that precise positioning of the ER could influence the duration, strength and direction of plasticity<sup>36–38</sup>. Naturally, further work (including improvement/development of new experimental techniques) is required to address this interesting hypothesis.

Another intriguing finding of our study concerns the role of spine ER in spine head  $\text{Ca}^{2+}$  homeostasis. We provide initial evidence that ER morphologies compensate for changes in spine morphology. This set of simulations also indicates that changes in ER morphology/volume in the area between the spine neck and spine head most effectively modulate  $\text{Ca}^{2+}$  signaling. Interestingly, the peak amplitude of the  $\text{Ca}^{2+}$  signal in the spine head but not the decay dynamics can be restored, specifically in the case of prolonged  $\text{Ca}^{2+}$  influx durations. This observation is attributed to a limited  $\text{Ca}^{2+}$  storage capacity, i.e., a rapid depletion of the intracellular store in our simulations, which “sharpens” the  $\text{Ca}^{2+}$  kinetics in the spine head. Whether this observation is relevant for ER-containing spines that undergo plasticity needs to be determined. It is also possible that additional molecular mechanisms may account for the limited  $\text{Ca}^{2+}$  capacity in order to maintain homeostasis, e.g., changes in SERCA and/or SOCE.

It is worth noting in this context that spine ER can assume peculiar morphological conformations that may resemble the herein described “spine-within-spine” ER morphology. The spine apparatus organelle is found in a subset of dendritic spines, consisting of stacked ER, which is typically located in the spine neck and head<sup>39–42</sup>. While its role in local protein synthesis is still debated, a link has been established between the spine apparatus and intracellular  $\text{Ca}^{2+}$  stores<sup>9,28,43–45</sup>. Indeed, using the actin-binding protein synaptopodin, which is a marker and essential component of the spine apparatus<sup>46,47</sup>, evidence has been provided that synaptopodin-associated  $\text{Ca}^{2+}$  transients from intracellular stores modulate the ability of neurons to express synaptic plasticity<sup>28,48–50</sup>. Similar to spine ER,

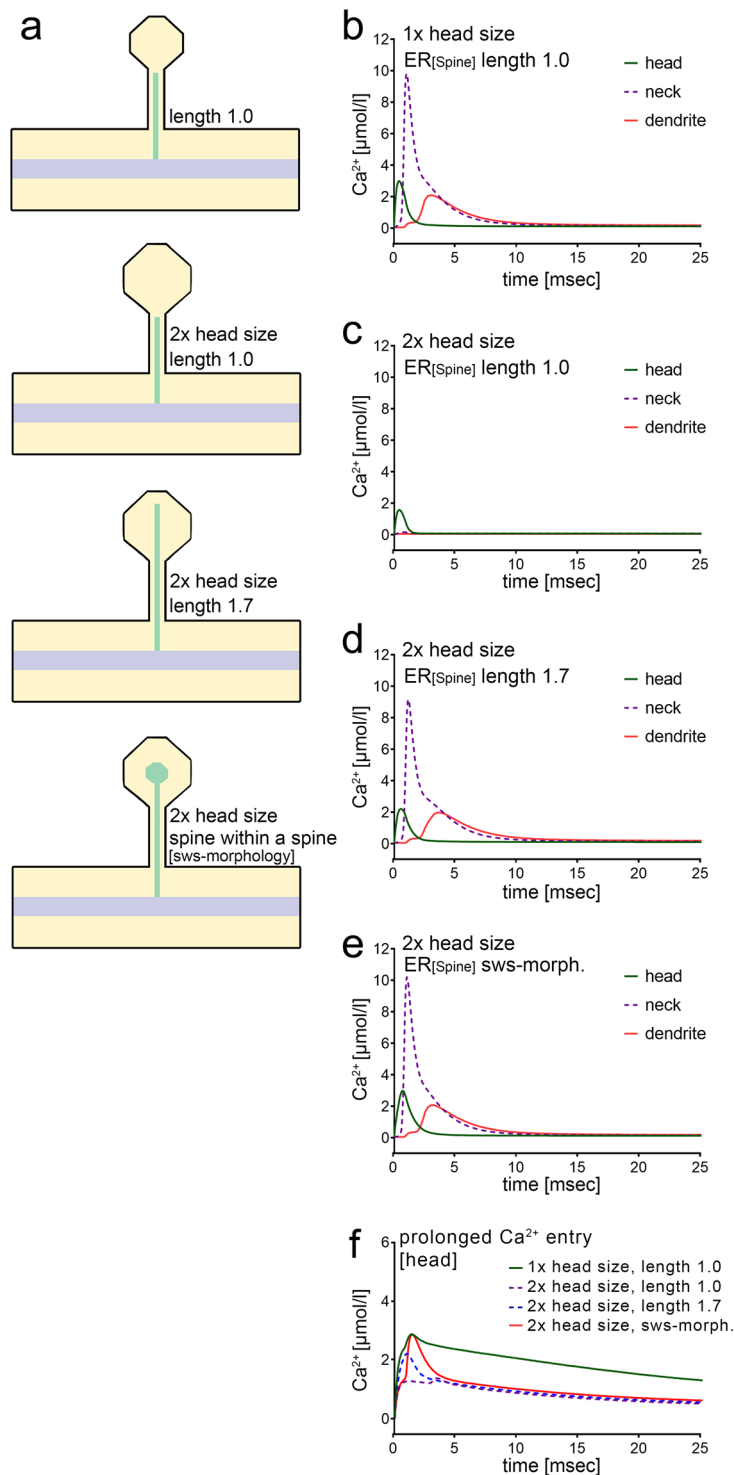


**Figure 6.** RyR-containing ER compensates increased spine head size. (a) Illustration of the ER morphologies used for the simulations in (b–e). (b,c) Increasing the spine head volume by a factor of 2 disables spine-to-dendrite Ca<sup>2+</sup> communication in response to a 1 ms Ca<sup>2+</sup> influx into the spine head. The peak [Ca<sup>2+</sup>] in the spine head is significantly reduced. (d) Increasing the ER length restores spine-to-dendrite communication. However, the original peak [Ca<sup>2+</sup>] in the head, neck, and dendrite cannot be restored to the original profiles in (b). (e) Introducing a widened terminal segment of the spine ER (“spine-within-spine” morphology) restores the original Ca<sup>2+</sup> profiles. (f) For simulations with 10 ms Ca<sup>2+</sup> release, the peak amplitude of the Ca<sup>2+</sup> signal in the spine head is also restored with the “spine-within-spine” ER morphology. The decay dynamics in the head, however, become sharper in comparison, due to depletion of the intracellular calcium store.

the spine apparatus appears to be a dynamic structure that leaves and enters individual spines<sup>28</sup> and changes its size, i.e., stack number<sup>51</sup>. Moreover, evidence has been provided that the spine apparatus is part of a  $\text{Ca}^{2+}$ -dependent negative-feedback mechanism mediating homeostatic synaptic plasticity<sup>51</sup> and that the size of spine apparatuses can change under pathological conditions such as systemic inflammation<sup>52</sup> or experimentally induced seizures<sup>53</sup>. Apparently, our current findings motivate a rigorous study of the importance of stacked, membrane-infolded ER architectures (potentially to increase a surface to volume ratio). We are confident that these future studies will shed new and important light on the relevance of ER conformation in  $\text{Ca}^{2+}$  wave segregation and propagation and may thus provide new insight into the functional significance of ER derivatives/specializations, such as spine apparatuses<sup>39,41,42</sup>, cisternal organelles<sup>54–60</sup>, or subsurface organelles in dendrites and cell bodies<sup>61–63</sup>.

While we addressed basic principles of spine ER reorganization using simplified morphologies in this study, it will now be important to also employ more complex, i.e., realistic spine and ER morphologies based on super-resolution microscopy and/or serial electron microscopy. These models should also consider complex synaptic activity, i.e., plasticity-inducing AMPA-R- and NMDA-R- and mGluR-mediated  $\text{Ca}^{2+}$  signals. Yet, the results of the present study show that the major conclusions are robust across various  $\text{Ca}^{2+}$  release profiles. Since more complex effects may arise, e.g., from local depletion of intracellular  $\text{Ca}^{2+}$  stores and ORAI-STIM1-mediated SOCE, it will be important to also integrate these findings into models that also account for dendritic, somatic and axonal ER configurations. It is well established that space-time integration of  $\text{Ca}^{2+}$  signals originating at multiple spines plays an important role in  $\text{Ca}^{2+}$  signaling toward the soma and nucleus<sup>64,65</sup>. Hence, it is conceivable that the precise nature of the timing and the waveform of synaptically induced  $\text{Ca}^{2+}$  signals are relevant not only for spine-to-dendrite communication, but also for inter-synaptic and synapse-to-nucleus communication. Thus, spine ER positioning along entire dendritic branches and within multiple synaptic spines must be considered. The nature of structure/function interplay demands an inclusion of the three-dimensional intracellular architecture in order to capture the ways in which cellular organization can influence biochemical (and potentially electrical<sup>66</sup>) signals. The parametric geometry design approach developed for this study was included in the simulation toolbox NeuroBox<sup>20</sup>. This modular framework could be extended for future studies on more complex surface/volume/distance law models that integrate and test for the relevance of complex activity patterns on spine, dendrite and somatic ER morphologies in  $\text{Ca}^{2+}$  homeostasis and synapse-to-nucleus communication.

## Methods

All necessary components were implemented in the simulation toolbox NeuroBox<sup>20</sup>.

**NeuroBox spine generator.** NeuroBox is a simulation toolbox that combines models of electrical and biochemical signaling on one- to three-dimensional computational domains. NeuroBox allows the definition of model equations, typically formulated as ordinary and partial differential equations, of the cellular computational domain and specification of the mathematical discretization methods and solvers<sup>67</sup>. Built with VRL-Studio<sup>68</sup>, NeuroBox offers user interface workflow canvases to control the simulation workflow and all biological and numerical parameters.

A novel spine generator using a parametric design approach was developed and implemented in NeuroBox, that allowed us to systematically vary the morphology of a spine (as well as the endoplasmic reticulum) and study its influence on the intracellular  $\text{Ca}^{2+}$  dynamics (see Sec. “model equations”–“membrane transport mechanisms”). The resulting partial differential equations with membrane mechanisms on the endoplasmic and plasma membrane were solved using a finite volume discretization and a parallel iterative solver (see Sec. “numerical methods”).

In the numerical simulation framework UG 4<sup>67</sup>, a computational domain  $\Omega \in \mathbb{R}^n$ ,  $n \in \{1, 2, 3\}$ , is represented by a piecewise linear approximation  $\Omega_h$  (“grid”). All grid-related data structures and algorithms are implemented in the UG 4 core library *lib\_grid* which also constitutes the basis for the UG 4 plugin and cross-platform meshing software ProMesh<sup>69,70</sup>. *lib\_grid* features state-of-the-art grid generation data structures and algorithms which were incorporated in a consecutive workflow to automatically construct 3D grid variations of a dendritic segment including the ER and spine with corresponding spine ER. To this end, the spine generator utilizes the *lib\_grid* functionality for basic geometric element initialization and manipulation, i.e., insertion/deletion of vertices, edges, faces and volumes, as well as translation and scaling. Furthermore, composite functions for creating and extruding simple geometric objects like circles, as well as sophisticated grid generation algorithms for constrained Delaunay tetrahedrization<sup>71,72</sup> are accessed in the ProMesh plugin. A Delaunay tetrahedrization  $\mathcal{S} = \{T_1, \dots, T_M\}$  is a special kind of tetrahedrization in which every tetrahedron  $T_i$  complies with the *Delaunay condition*, i.e., the unique circumsphere of each  $T_i$ , which passes through the four tetrahedral vertices, does not contain any vertices of the grid in its interior (Fig. 1d). This leads to high-quality grids which avoid tetrahedra with particularly acute or obtuse interior angles<sup>73</sup>, an essential grid property for accurate approximation and fast solution in numerical simulation<sup>74–76</sup>.

The user can specify 10 characteristic geometric parameters to specify the individual morphology of the spine grid output (Table 1). The generated grids are written to the native UG 4 file format UGX and can be viewed and modified using the GUI version of ProMesh. The fundamental workflow can be summarized as follows:

1. The exterior dendrite and interior ER structures are constructed around the origin (0.0, 0.0, 0.0) using the ProMesh create-circle approximation with a chosen default resolution of 8 rim vertices and user-specified radii (Fig. 1e).
2. The dendritic and ER circles, respectively, are then successively extruded along the z-axis while at the same time creating quadrilateral faces enclosing the emerging cylinder barrels using user-specified lengths (Fig. 1f).

3. The previous process is interrupted by an in-between extrusion step for creating a measurement zone of user-specified spine neck length around the spine ER placed at the user-specified z-coordinate for the spine position.
4. At the z-coordinate for the spine position, spine ER and neck are generated by a circular remeshing of the local ER and dendritic surface grid, and subsequent extrusion along the y-axis, creating quadrilateral faces enclosing the emerging cylinder barrels using specified lengths.
5. The spine head is placed on top of the neck by continued extrusion along the y-axis. Subsequently, the cylindrical spine head vertices are projected to spherical coordinates around the head barycenter using the head radius.
6. The remaining planar holes at the dendrite and ER cylinder top and bottom are triangulated to close the encapsulated surface geometry (Fig. 1g).
7. Surface elements are selected automatically by their coordinates in order to be assigned to individual subsets for access during numerical simulation.
8. Given the piecewise linear closed and encapsulated surface geometry, the corresponding volume grid is generated using constrained Delaunay tetrahedrization allowing for an individual subset assignment of tetrahedral elements which are separated by lower dimensional subsets.

**Model equations.** Three-dimensional spatio-temporal  $\text{Ca}^{2+}$  and inositol trisphosphate ( $\text{IP}_3$ ) dynamics in the intracellular space are modeled by a system of diffusion-reaction equations described in the following. The boundary conditions for this partial differential equation system are specified by  $\text{Ca}^{2+}$  - and  $\text{IP}_3$ -dependent flux boundary conditions described in Sec. “Membrane transport mechanisms”.

The model considers the quantities *calcium* (cytosolic ( $c_c$ ) and endoplasmic ( $c_e$ )), *calbindin- $D_{28k}$*  ( $b$ ), and  $\text{IP}_3$  ( $p$ ), which is required to model  $\text{IP}_3$  receptors embedded in the endoplasmic membrane. Mobility in the cytosol/ER is described by the diffusion equation

$$\frac{\partial u}{\partial t} = \nabla \cdot (D \nabla u) \quad (1)$$

where  $u(x, t)$  stands for the the four quantities mentioned above. The diffusion constants  $D$  are defined using data from<sup>77,78</sup>.

The interaction between cytosolic  $\text{Ca}^{2+}$  and calbindin- $D_{28k}$  (CalB) is described by



The rate constants  $\kappa_b^-$  and  $\kappa_b^+$  are given in Table 2. While CalB has four distinct high-affinity  $\text{Ca}^{2+}$ -binding sites<sup>79</sup>, we currently treat it as though it had only one, at the same time quadrupling its concentration in our model. This amounts to assuming that all four binding sites are essentially equal and binding is non-cooperative (though data by<sup>80,81</sup> indicate this might not necessarily be the case).

The equations for cytosolic  $\text{Ca}^{2+}$  and CalB are thus given by

$$\frac{\partial c_c}{\partial t} = D_c \Delta c_c + (\kappa_b^- (b^{\text{tot}} - b) - \kappa_b^+ b c_c), \quad (3)$$

$$\frac{\partial b}{\partial t} = D_b \Delta b + (\kappa_b^- (b^{\text{tot}} - b) - \kappa_b^+ b c_c) \quad (4)$$

in the cytosolic domain, where the concentration of the CalB- $\text{Ca}^{2+}$  compound is expressed by the difference of the total concentration of CalB present in the cytosol ( $b^{\text{tot}}$ ) and free CalB, the former of which is assumed to be constant in space and time (this amounts to the assumption that free and  $\text{Ca}^{2+}$ -binding CalB have the same diffusive properties). All parameters are listed in Table 2.

Exponential  $\text{IP}_3$  decay towards a basal  $\text{IP}_3$  concentration  $p^r$  in the cytosolic space is modeled by a reaction term that is added to the  $\text{IP}_3$  diffusion equation, leading to the diffusion-reaction equation

$$\frac{\partial p}{\partial t} = D_p \Delta p - \kappa_p (p - p^r) \quad (5)$$

for  $\text{IP}_3$  in the cytosolic domain. Endoplasmic  $\text{Ca}^{2+}$  dynamics are modeled by simple diffusion

$$\frac{\partial c_e}{\partial t} = D_e \Delta c_e \quad (6)$$

in the endoplasmic domain.

**Membrane transport mechanisms.** In order to study the influence of intracellular organization on  $\text{Ca}^{2+}$  signals, we include  $\text{Ca}^{2+}$  exchange mechanisms on the endoplasmic membrane (ERM) and the plasma membrane (PM).  $\text{IP}_3$  receptors ( $\text{IP}_3\text{R}$ ), ryanodine receptors (RyR), sarco/endoplasmic reticulum  $\text{Ca}^{2+}$ -ATPase pumps (SERCA) as well as a leakage term are modeled to describe the bi-directional exchange of  $\text{Ca}^{2+}$  across the ER membrane. For the plasma membrane we consider plasma membrane  $\text{Ca}^{2+}$ -ATPase pumps (PMCA),  $\text{Na}^+/\text{Ca}^{2+}$  exchangers (NCX) and a leakage term. This amounts to the flux equations

$$j_{\text{ERM}} = j_I + j_R - j_S + j_{l,e}, \quad (7)$$

$$j_{\text{PM}} = -j_P - j_N + j_{l,p}. \quad (8)$$

where  $j_I$  is the IP<sub>3</sub>R flux density,  $j_R$  the RyR flux density,  $j_S$  the SERCA flux density and  $j_{l,e}$  the leakage flux density on the ERM, and  $j_P$ ,  $j_N$  and  $j_{l,p}$  the flux densities of PMCA, NCX, and leakage flux density of the PM, respectively. Homogeneous distributions of all exchange mechanisms were assumed, as experimental data on precise numbers and spatio-temporal distribution of these receptors within individual spines are not available.

**IP<sub>3</sub>R channels.** The flux density  $j_I$  (number of ions per membrane area and time) through the ER membrane is calculated by

$$j_I = \rho_I \cdot p_I^o \cdot I_I, \quad (9)$$

where  $\rho_I$  is the density of IP<sub>3</sub> receptors in the ER membrane,  $p_I^o$  is the open state probability of a single channel, and  $I_I$  the single channel Ca<sup>2+</sup> current.

The single channel current model is based on<sup>82</sup>, where experimental data are fitted by a Michaelis-Menten equation, and is quasi-linear in the physiologically relevant range for luminal Ca<sup>2+</sup> concentrations (and below). Thus, we chose

$$I_I = I_I^{\text{ref}} \frac{c_e - c_c}{c_e^{\text{ref}}} \quad (10)$$

with a reference concentration  $c_e^{\text{ref}}$  well inside the admissible range.

For the open state probability, we used the model from<sup>83</sup>:

$$p_I^o = \left( \frac{d_2 c_d p}{(c_d p + d_2 p + d_3 c_c + d_1 d_2)(c_c + d_5)} \right)^3 \quad (11)$$

with kinetic parameters  $d_1$ ,  $d_2$ ,  $d_3$  and  $d_5$  (see Table 2).

**RyR channels.** Similar to the IP<sub>3</sub>R channels, the Ca<sup>2+</sup> flux density generated by ryanodine receptor channels at the ER membrane is given by an expression of the form

$$j_R = \rho_R \cdot p_R^o \cdot I_R, \quad (12)$$

where  $\rho_R$  is the density of RyR in the ER membrane,  $p_R^o$  is the open state probability of a single channel, and  $I_R$  the single channel Ca<sup>2+</sup> current.

Using the approach from<sup>84</sup>, we describe the single channel ionic current by

$$I_R = I_R^{\text{ref}} \frac{c_e - c_c}{c_e^{\text{ref}}}, \quad (13)$$

where the reference current  $I_R^{\text{ref}}$  is approximated from data presented in<sup>85</sup>.

The open probability for RyR channels is taken from<sup>84</sup> and can be calculated as the sum of the two open states  $o_1$  and  $o_2$  in the system of ordinary differential equations

$$o_1 = 1 - c_1 - o_2 - c_2 \quad (14)$$

$$\frac{\partial c_1}{\partial t} = k_a^- o_1 - k_a^+ c_c^4 c_1 \quad (15)$$

$$\frac{\partial o_2}{\partial t} = k_b^+ c_c^3 o_1 - k_b^- o_2 \quad (16)$$

$$\frac{\partial c_2}{\partial t} = k_c^+ o_1 - k_c^- c_2 \quad (17)$$

with the kinetic constants  $k_a^\pm$ ,  $k_b^\pm$  and  $k_c^\pm$  (see Table 2), that can be solved independently for every point on the surface of the ER membrane.

**SERCA pumps.** The current from sarco/endoplasmic reticulum Ca<sup>2+</sup>-ATPase pumps is described by a model from<sup>86</sup>, which was adapted for the three-dimensional case, and gives rise to the Ca<sup>2+</sup> flux density

$$j_S = \rho_S \cdot \frac{I_S c_c}{(K_S + c_c) c_c}. \quad (18)$$

The model reflects the dependence of the  $\text{Ca}^{2+}$  current not only on the cytosolic concentration but also on the endoplasmic saturation. Parameter specifications can be found in Table 2.

**PMCA pump.** Using the model presented by<sup>87</sup>, we model the plasma membrane  $\text{Ca}^{2+}$ -ATPase current as a second-order Hill-equation

$$j_p = \rho_p \cdot \frac{I_p c_c^2}{K_p^2 + c_c^2}. \quad (19)$$

All parameters are listed in Table 2.

**NCX pump.** For the  $\text{Na}^+/\text{Ca}^{2+}$  exchanger current, we assume a constant  $\text{Na}^+$  concentration at the plasma membrane, following the first-order Hill-equation used in<sup>87</sup>:

$$j_N = \rho_N \cdot \frac{I_N c_c}{K_N + c_c}. \quad (20)$$

All parameters are listed in Table 2.

**Leakage.** Both the ERM and the PM allow a leakage flux not accounted for by the above transport mechanisms. These leakage fluxes are calibrated to ensure zero membrane net flux in the equilibrium state for all simulated ions and agents. Leakage flux densities are modeled by

$$j_{l,e} = v_{l,e} \cdot (c_e - c_c), \quad (21)$$

$$j_{l,p} = v_{l,p} \cdot (c_o - c_c), \quad (22)$$

where  $c_o$  is the extracellular  $\text{Ca}^{2+}$  concentration, which is assumed to be constant throughout all simulations.

**Calcium release and  $\text{IP}_3$  production.** Calcium release is modeled as a Neumann boundary condition for the cytosolic  $\text{Ca}^{2+}$  concentration, i.e., a time-dependent influx density function defined at the postsynaptic membrane. The 1 ms release is modeled by a linearly decreasing  $\text{Ca}^{2+}$  pulse of 1 ms duration starting at an initial maximal specific current density  $j_c^{\text{rls}}$ . The 10 ms calcium release profile was modeled as a decaying exponential influx

$$j_c^{\text{rls}} \exp\left(-\frac{t}{\tau_{\text{rls}}}\right) \quad (23)$$

with a decay constant  $\tau_{\text{rls}} = 10$  ms. The prolonged calcium release was modeled by an NMDA receptor model that defined a flux with time constant  $\tau_{\text{NMDAR}} = 150$  ms:

$$j_{\text{NMDAR}} = \rho_{\text{NMDAR}} p_{\text{max}}^o \exp\left(-\frac{t}{\tau_{\text{NMDAR}}}\right) \cdot I_{\text{NMDAR}}, \quad (24)$$

where  $\rho_{\text{NMDAR}}$  is the density of NMDARs in the postsynaptic membrane,  $p_{\text{max}}^o$  is the maximal single-channel open probability, and the single-channel ionic current  $I_{\text{NMDAR}}$  is given by the Goldman-Hodgkin-Katz expression

$$I_{\text{NMDAR}} = p_{\text{NMDAR}} \cdot \frac{V_m}{\tilde{V}} \cdot \frac{c_o - c_c \exp\left(\frac{V_m}{\tilde{V}}\right)}{1.0 - \exp\left(\frac{V_m}{\tilde{V}}\right)}. \quad (25)$$

The product  $\rho_{\text{NMDAR}} p_{\text{max}}^o$  was calibrated such that the maximal expected number of open channels in the spine was one<sup>88</sup>. The permeability  $p_{\text{NMDAR}}$  was set to a value that results in a single-channel current in accordance with data published by Jahr and Stevens<sup>89</sup>. We supposed a constant membrane potential value  $V_m = -70$  mV and used the fact that approximately 10% of the current through NMDARs is carried by  $\text{Ca}^{2+}$  at 2 mM extracellular  $\text{Ca}^{2+}$  concentrations<sup>89</sup>. We took into account the  $\text{Mg}^{2+}$  block that reduces the channel conductance by a factor of about twenty<sup>90</sup> at physiological 0.7 mM extracellular  $\text{Mg}^{2+}$  concentrations<sup>91</sup>.

The production of  $\text{IP}_3$  is also modeled as an “influx” (as it is produced at the plasma membrane) decaying linearly over the course of 200 ms from a specific current density  $j_p^{\text{rls}}$ . Since we only simulate on a portion of the dendrite at the base of a single spine, we do not capture diffusion across the dendritic boundaries of our geometry. While this is irrelevant for fast-buffered calcium,  $\text{IP}_3$  can diffuse farther and is eventually constrained by the geometric boundaries. Over time this would lead to unrealistically high accumulation of  $\text{IP}_3$ . To adjust for this effect,  $\text{IP}_3$  production was reduced compared to<sup>92</sup>.

Values for all model parameters are gathered in Table 2.

**Numerical Methods.** For numerical simulations, the four equations are discretized in space using a finite volumes method. Current densities, both synaptic and across the ER and plasma membranes, can be incorporated

into the reaction-diffusion process very naturally and easily this way. We show how this is achieved using the cytosolic  $\text{Ca}^{2+}$  Eq. (3) as an example: It is reformulated (using the divergence theorem) to an integral version

$$\int_B \frac{\partial c_c}{\partial t} dV = \int_{\partial B} D_c \nabla^T c_c \cdot n_{\partial B} dS + \int_B (\kappa_b^- (b^{\text{tot}} - b) - \kappa_b^+ b c_c) dV, \quad (26)$$

where  $B$  is a control volume that will be specified shortly, and  $n_{\partial B}$  is the outward normal on the boundary of  $B$ . For control volumes located at the ER membrane, some portion of its boundary will coincide with the ER membrane. Since there is no diffusive flux density  $D_c \nabla^T c_c$  across the ER membrane, we can simply substitute it by the ER flux density  $j_{\text{ERM}}$  as given in (7) in the boundary integral for this portion of the boundary. The same applies to the plasma membrane and the synapse area. The diffusive flux is set to zero on the rest of the cytosolic domain boundary. If we denote the cytosolic boundary by  $\Gamma$ , its ER/plasma membrane and synaptic parts by  $\Gamma_{\text{ERM}}$ ,  $\Gamma_{\text{PM}}$  and  $\Gamma_{\text{syn}}$  respectively, this yields the following equation:

$$\begin{aligned} \int_B \frac{\partial c_c}{\partial t} dV = & \int_{\partial B \cap \Gamma} D_c \nabla^T c_c \cdot n_{\partial B} dS + \int_{\partial B \cap \Gamma_{\text{ERM}}} j_{\text{ERM}}^T \cdot n_{\partial B} dS \\ & + \int_{\partial B \cap \Gamma_{\text{PM}}} j_{\text{PM}}^T \cdot n_{\partial B} dS + \int_{\partial B \cap \Gamma_{\text{syn}}} j_{\text{syn}}^T \cdot n_{\partial B} dS \\ & + \int_B (\kappa_b^- (b^{\text{tot}} - b) - \kappa_b^+ b c_c) dV. \end{aligned} \quad (27)$$

Control volumes are constructed as a Voronoi-like dual tessellation of the original tetrahedral mesh by connecting the mid-points of edges, faces and volumes through planar facets. Equation (27) must hold for all control volumes, giving rise to one equation per control volume.

Time discretization is realized using a backwards Euler scheme, i.e., for each point in time  $t$ , the term  $\frac{\partial c_c}{\partial t}$  in (27) is replaced by the discretized term  $\frac{c_c(t) - c_c(t - \tau)}{\tau}$  and all quantities on the right-hand side are evaluated at time  $t$ . Here,  $\tau$  is the time step size of the time discretization.

By limiting the function space to the space of continuous functions that are linear on all volumes of the original mesh, the integrals in Eq. (27) can be evaluated efficiently. Moreover, the solution can be represented by one degree of freedom per volume, so there is one equation for each degree of freedom. The system of equations arising from this procedure is nonlinear (due to the nonlinear reaction term and, more importantly, the highly nonlinear transport terms across the membranes) and is therefore linearized by a Newton iteration.

For the results we present here, the emerging linearized problems were solved using a Bi-CGSTAB<sup>93</sup> linear solver preconditioned by an incomplete LU decomposition. Computations were facilitated by a domain decomposition parallelization approach and carried out using the UG 4 framework<sup>67</sup> on the JURECA computer system at the Jülich Supercomputing Centre<sup>94</sup>.

## References

- Porter, K. Observations on a submicroscopic basophilic component of cytoplasm. *J Exp Med* **97**, 727–750 (1953).
- Verkhratsky, A. Physiology and pathophysiology of the calcium store in the endoplasmic reticulum of neurons. *Physiol. Rev.* **85**, 201–279, <https://doi.org/10.1152/physrev.00004.2004>, <http://physrev.physiology.org/content/85/1/201.full.pdf> (2004).
- Stutzmann, G. E. & Mattson, M. P. Endoplasmic reticulum  $\text{Ca}^{2+}$  handling in excitable cells in health and disease. *Pharmacol. Rev.* **63**, 700–727, <https://doi.org/10.1124/pr.110.003814>, <http://pharmrev.aspetjournals.org/content/63/3/700.full.pdf> (2011).
- Friedman, J. & Voeltz, G. The ER in 3D: a multifunctional dynamic membrane network. *Trends Cell Biol* **21**, 709–717 (2011).
- Berridge, M. Neuronal calcium signaling. *Neuron* **21**, 13–26 (1998).
- Segal, M. & Korkotian, E. Endoplasmic reticulum calcium stores in dendritic spines. *Front. Neuroanat.* **8**, 64, <http://journal.frontiersin.org/article/10.3389/fnana.2014.00064>, <https://doi.org/10.3389/fnana.2014.00064> (2014).
- Maggio, N. & Vlachos, A. Synaptic plasticity at the interface of health and disease: New insights on the role of endoplasmic reticulum intracellular calcium stores. *Neurosci.* **281**, 135–146, <http://www.sciencedirect.com/science/article/pii/S0306452214007921>, <https://doi.org/10.1016/j.neuroscience.2014.09.041> (2014).
- Finch, E. A., Tanaka, K. & Augustine, G. J. Calcium as a trigger for cerebellar long-term synaptic depression. *The Cerebellum* **11**, 706–717, <https://doi.org/10.1007/s12311-011-0314-x> (2012).
- Jedlicka, P. & Deller, T. Understanding the role of synaptopodin and the spine apparatus in Hebbian synaptic plasticity – New perspectives and the need for computational modeling. *Neurobiol. Learn. Mem.* **138**, 21–30, <http://www.sciencedirect.com/science/article/pii/S107474271630123X>, <https://doi.org/10.1016/j.nlm.2016.07.023>. MCCS 2017 (2017).
- Sharp, A. *et al.* Differential immunohistochemical localization of inositol 1, 4, 5-trisphosphate- and ryanodine-sensitive  $\text{Ca}^{2+}$  release channels in rat brain. *J. Neurosci.* **13**, 3051–3063, <http://www.jneurosci.org/content/13/7/3051.full.pdf> (1993).
- Holbro, N., Grunditz, Å. & Oertner, T. G. Differential distribution of endoplasmic reticulum controls metabotropic signaling and plasticity at hippocampal synapses. *Proc. Natl. Acad. Sci.* **106**, 15055–15060, <https://doi.org/10.1073/pnas.0905110106>, <http://www.pnas.org/content/106/35/15055.full.pdf> (2009).
- Goto, J.-I. & Mikoshiba, K. Inositol 1, 4, 5-trisphosphate receptor-mediated calcium release in Purkinje cells: from molecular mechanism to behavior. *The Cerebellum* **10**, 820–833, <https://doi.org/10.1007/s12311-011-0270-5> (2011).
- Rose, C. R. & Konnerth, A. Stores not just for storage. *Neuron* **31**, 519–522, <http://www.sciencedirect.com/science/article/pii/S0896627301004020>, [https://doi.org/10.1016/S0896-6273\(01\)00402-0](https://doi.org/10.1016/S0896-6273(01)00402-0) (2001).
- Dittmer, P. J., Wild, A. R., Dell'Acqua, M. L. & Sather, W. A. STIM1  $\text{Ca}^{2+}$  sensor control of L-type  $\text{Ca}^{2+}$ -channel-dependent dendritic spine structural plasticity and nuclear signaling. *Cell Reports* **19**, 321–334, <http://www.sciencedirect.com/science/article/pii/S2211124717304175>, <https://doi.org/10.1016/j.celrep.2017.03.056> (2017).
- Tshuva, R. Y., Korkotian, E. & Segal, M. ORA11-dependent synaptic plasticity in rat hippocampal neurons. *Neurobiol. Learn. Mem.* **140**, 1–10, <http://www.sciencedirect.com/science/article/pii/S1074742716303483>, <https://doi.org/10.1016/j.nlm.2016.12.024> (2017).
- Toresson, H. & Grant, S. G. N. Dynamic distribution of endoplasmic reticulum in hippocampal neuron dendritic spines. *Eur. J. Neurosci.* **22**, 1793–1798, <https://doi.org/10.1111/j.1460-9568.2005.04342.x> (2005).
- Ng, A. N. & Toresson, H. Endoplasmic reticulum dynamics in hippocampal dendritic spines induced by agonists of type I metabotropic glutamate but not by muscarinic acetylcholine receptors. *Synapse* **65**, 351–355, <https://doi.org/10.1002/syn.20887> (2011).

18. Biess, A., Korkotian, E. & Holzman, D. Diffusion in a dendritic spine: The role of geometry. *Phys. Rev. E* **76**, 021922, <https://doi.org/10.1103/Phys-RevE.76.021922> (2007).
19. Yasuda, R. Biophysics of biochemical signaling in dendritic spines: Implications in synaptic plasticity. *Biophys. J.* **113**, 2152–2159, <http://www.sciencedirect.com/science/article/pii/S000634951730855X>, <https://doi.org/10.1016/j.bpj.2017.07.029> (2017).
20. Breit, M. *et al.* Anatomically detailed and large-scale simulations studying synapse loss and synchrony using NeuroBox. *Front. Neuroanat.* **10**, 8, <https://doi.org/10.3389/fnana.2016.00008> (2016).
21. Tonnesen, J., Katona, G., Rózsa, B. & Nägerl, U. V. Spine neck plasticity regulates compartmentalization of synapses. *Nat. Neurosci.* **17**, 678–685, <https://doi.org/10.1038/nn.3682> (2014).
22. Sabatini, B. L., Oertner, T. G. & Svoboda, K. The life cycle of Ca<sup>2+</sup> ions in dendritic spines. *Neuron* **33**, 439–452, <http://www.sciencedirect.com/science/article/pii/S0896627302005731>, [https://doi.org/10.1016/S0896-6273\(02\)00573-1](https://doi.org/10.1016/S0896-6273(02)00573-1) (2002).
23. Reyes, M. & Stanton, P. Induction of hippocampal long-term depression requires release of Ca<sup>2+</sup> from separate presynaptic and postsynaptic intracellular stores. *J. Neurosci.* **16**, 5951–5960 (1996).
24. Nishiyama, M., Hong, K., Mikoshiba, K., Poo, M. M. & Kato, K. Calcium stores regulate the polarity and input specificity of synaptic modification. *Nat.* **408**, 584–588 (2000).
25. Feldman, D. E. The spike-timing dependence of plasticity. *Neuron* **75**, 556–571 (2012).
26. Markram, H., Gerstner, W. & Sjöström, P. A history of spike-timing-dependent plasticity. *Front. Synaptic Neurosci.* **3**, <https://doi.org/10.3389/fnsyn.2011.00004> (2011).
27. Dan, Y. & Poo, M. Spike timing-dependent plasticity: from synapse to perception. *Physiol. Rev.* **86**, 1033–1048, <https://doi.org/10.1152/physrev.00030.2005> (2006).
28. Vlachos, A. *et al.* Synaptopodin regulates plasticity of dendritic spines in hippocampal neurons. *J. Neurosci.* **29**, 1017–1033, <https://doi.org/10.1523/JNEUROSCI.5528-08.2009>, <http://www.jneurosci.org/content/29/4/1017.full.pdf> (2009).
29. Matsuzaki, M., Honkura, N., Ellis-Davies, G. & Kasai, H. Structural basis of long-term potentiation in single dendritic spines. *Nat.* **429**, 761–766 (2004).
30. Bosch, M. *et al.* Structural and molecular remodeling of dendritic spine substructures during long-term potentiation. *Neuron* **82**, 444–459, <https://doi.org/10.1016/j.neuron.2014.03.021> (2014).
31. Sabatini, B., Maravall, M. & Svoboda, K. Ca(2+) signaling in dendritic spines. *Curr. Opin. Neurobiol.* **11**, 349–356, <https://www.ncbi.nlm.nih.gov/pubmed/?term=sabatini+bl+2001> (2001).
32. Kovalchuk, Y., Eilers, J., Lisman, J. & Konnerth, A. NMDA receptor-mediated subthreshold Ca(2+) signals in spines of hippocampal neurons. *J. Neurosci.* **20**, 1791–1799, <https://www.ncbi.nlm.nih.gov/pubmed/?term=kovalchuk+2000+calcium> (2000).
33. Mainen, Z., Malinow, R. & Svoboda, K. Synaptic calcium transients in single spines indicate that NMDA receptors are not saturated. *Nat.* **399**, 151–155, <https://www.ncbi.nlm.nih.gov/pubmed/10335844> (1999).
34. Emptage, N. Calcium on the up: supralinear calcium signaling in central neurons. *Neuron* **24**, 495–497, <https://www.ncbi.nlm.nih.gov/pubmed/10595500> (1999).
35. Emptage, N. Roles of calcium stores and store-operated channels in plasticity of dendritic spines. *Neurosci.* **22**, 477–485, <https://www.ncbi.nlm.nih.gov/pubmed/26511041>, <https://doi.org/10.1177/1073858415613277> (2016).
36. Abraham, W. & Bear, M. Metaplasticity: the plasticity of synaptic plasticity. *Trends Neurosci.* **19**, 126–130 (1996).
37. Abraham, W. Metaplasticity: tuning synapses and networks for plasticity. *Nat. Rev. Neurosci.* **9**, 387 (2008).
38. Hulme, S. R., Jones, O. D. & Abraham, W. C. Emerging roles of metaplasticity in behaviour and disease. *Trends Neurosci.* **36**, 353–362, <https://doi.org/10.1016/j.tins.2013.03.007> (2013).
39. Gray, E. G. Axo-somatic and axo-dendritic synapses of the cerebral cortex: An electron microscope study. *J. Anat.* **93**, 420–433, <http://www.ncbi.nlm.nih.gov/pmc/articles/PMC1244535/> (1959).
40. Hanus, C. & Ehlers, M. D. Secretory outposts for the local processing of membrane cargo in neuronal dendrites. *Traffic* **9**, 1437–1445, <https://doi.org/10.1111/j.1600-0854.2008.00775.x> (2008).
41. Spacek, J. Three-dimensional analysis of dendritic spines. II. Spine apparatus and other cytoplasmic components. *Anat. Embryol.* **171**, 235–243 (1985).
42. Spacek, J. & Harris, K. Three-dimensional organization of smooth endoplasmic reticulum in hippocampal CA1 dendrites and dendritic spines of the immature and mature rat. *J. Neurosci.* **17**, 190–203 (1997).
43. Fifkova, E., Markham, J. & Delay, R. Calcium in the spine apparatus of dendritic spines in the dentate molecular layer. *Brain Res.* **266**, 163–168 (1983).
44. Segal, M., Vlachos, A. & Korkotian, E. The spine apparatus, synaptopodin, and dendritic spine plasticity. *The Neurosci.* **16**, 125–131, <https://doi.org/10.1177/1073858409355829> PMID: 20400711 (2010).
45. Korkotian, E. & Segal, M. Synaptopodin regulates release of calcium from stores in dendritic spines of cultured hippocampal neurons. *The J. Physiol.* **589**, 5987–5995, <https://doi.org/10.1113/jphysiol.2011.217315> (2011).
46. Mundel, P. *et al.* Synaptopodin: an actin-associated protein in telencephalic dendrites and renal podocytes. *The J. Cell Biol.* **139**, 193–204, <https://doi.org/10.1083/jcb.139.1.193>, <http://jcb.rupress.org/content/139/1/193.full.pdf> (1997).
47. Deller, T., Merten, T., Roth, S. U., Mundel, P. & Frotscher, M. Actin-associated protein synaptopodin in the rat hippocampal formation: Localization in the spine neck and close association with the spine apparatus of principal neurons. *The J. Comp. Neurol.* **418**, 164–181 (2000).
48. Deller, T. *et al.* Synaptopodin-deficient mice lack a spine apparatus and show deficits in synaptic plasticity. *Proc. Natl. Acad. Sci.* **100**, 10494–10499, <https://doi.org/10.1073/pnas.1832384100>, <http://www.pnas.org/content/100/18/10494.full.pdf> (2003).
49. Jedlicka, P. *et al.* Impairment of *in vivo* theta-burst long-term potentiation and network excitability in the dentate gyrus of synaptopodin-deficient mice lacking the spine apparatus and the cisternal organelle. *Hippocampus* **19**, 130–140, <https://doi.org/10.1002/hipo.20489> (2009).
50. Korkotian, E., Frotscher, M. & Segal, M. Synaptopodin regulates spine plasticity: mediation by calcium stores. *J. Neurosci.* **34**, 11641–11651, <https://doi.org/10.1523/JNEUROSCI.0381-14.2014>, <http://www.jneurosci.org/content/34/35/11641.full.pdf> (2014).
51. Vlachos, A. *et al.* Synaptopodin regulates denervation-induced homeostatic synaptic plasticity. *Proc. Natl. Acad. Sci.* **110**, 8242–8247, <https://doi.org/10.1073/pnas.1213677110>, <http://www.pnas.org/content/110/20/8242.full.pdf> (2013).
52. Strehl, A. *et al.* Systemic inflammation is associated with a reduction in synaptopodin expression in the mouse hippocampus. *Exp. Neurol.* **261**, 230–235, <http://www.sciencedirect.com/science/article/pii/S0014488614001484>, <https://doi.org/10.1016/j.expneurol.2014.04.033> (2014).
53. Lenz, M., Ben Shimon, M., Deller, T., Vlachos, A. & Maggio, N. Pilocarpine-induced status epilepticus is associated with changes in the actin-modulating protein synaptopodin and alterations in long-term potentiation in the mouse hippocampus. *Neural Plast.* **2017**, 7, <https://doi.org/10.1155/2017/2652560> (2017).
54. Palay, S., Sotelo, C., Peters, A. & Orkand, P. The axon hillock and the initial segment. *J. Cell Biol.* **38**, 193–201 (1968).
55. Somogyi, P. & Hamori, J. A quantitative electron microscopic study of the Purkinje cell axon initial segment. *Neurosci.* **1**, 361–365 (1976).
56. Kosaka, T. The axon initial segment as a synaptic site: ultrastructure and synaptology of the initial segment of the pyramidal cell in the rat hippocampus (CA3 region). *J. Neurocytol.* **9**, 861–882 (1980).
57. Lindsey, J. & Ellisman, M. The neuronal endomembrane system. III. *the origins of the axoplasmic reticulum and discrete axonal cisternae at the axon hillock.* *J. Neurosci.* **5**, 3135–3144 (1985).

58. Bas Orth, C., Schultz, C., Müller, C., Frotscher, M. & Deller, T. Loss of the cisternal organelle in the axon initial segment of cortical neurons in synaptopodin-deficient mice. *J Comp Neurol* **504**, 441–449 (2007).
59. Rasband, M. The axon initial segment and the maintenance of neuronal polarity. *Nat Rev Neurosci* **11**, 552–562 (2010).
60. Schlüter, A. *et al.* Structural plasticity of synaptopodin in the axon initial segment during visual cortex development. *Cereb. Cortex* **27**, 4662–4675, <https://doi.org/10.1093/cercor/bhx208> (2017).
61. Rosenbluth, J. Subsurface cisterns and their relationship to the neuronal plasma membrane. *J Cell Biol* **13**, 405–421 (1962).
62. Takahashi, K. & Wood, R. Subsurface cisterns in the Purkinje cells of cerebellum of Syrian hamster. *Z Zellforsch Mikrosk Anat* **110**, 311–320 (1970).
63. Gallart-Palau, X. *et al.* Neuregulin-1 is concentrated in the postsynaptic subsurface cistern of C-bouton inputs to a-motoneurons and altered during motoneuron diseases. *FASEB* **28**, 3618–3662 (2014).
64. Wittmann, M. *et al.* Synaptic activity induces dramatic changes in the geometry of the cell nucleus: interplay between nuclear structure, histone H3 phosphorylation, and nuclear calcium signaling. *J Neurosci* **29**, 14687–14700 (2009).
65. Lee, K. F., Soares, C., Thivierge, J.-P. & Béique, J.-C. Correlated synaptic inputs drive dendritic calcium amplification and cooperative plasticity during clustered synapse development. *Neuron* **89**, 784–799 <http://www.sciencedirect.com/science/article/pii/S0896627316000131>, <https://doi.org/10.1016/j.neuron.2016.01.012> (2016).
66. Cartiailler, J., Kwon, T., Yuste, R. & Holcman, D. Deconvolution of voltage sensor time series and electro-diffusion modeling reveal the role of spine geometry in controlling synaptic strength. *Neuron* <http://www.sciencedirect.com/science/article/pii/S089662731830059X>, <https://doi.org/10.1016/j.neuron.2018.01.034> (2018).
67. Vogel, A., Reiter, S., Rupp, M., Nägel, A. & Wittum, G. UG 4: A novel flexible software system for simulating PDE based models on high performance computers. *Comput. Vis. Sci.* **16**, 165–179, <https://doi.org/10.1007/s00791-014-0232-9> (2013).
68. Hoffer, M., Poliwoda, C. & Wittum, G. Visual reflection library: a framework for declarative GUI programming on the Java platform. *Comput. Vis. Sci.* **16**, 181–192, <https://doi.org/10.1007/s00791-014-0230-y> (2013).
69. Reiter, S. ProMesh – Meshing of unstructured grids in 1, 2, and 3 dimensions, <http://promesh3d.com> (2012).
70. Reiter, S. *Effiziente Algorithmen und Datenstrukturen für die Realisierung von adaptiven, hierarchischen Gittern auf massiv parallelen Systemen. Phd. thesis, Goethe-Universität Frankfurt am Main* (2014).
71. Shewchuk, J. Constrained Delaunay tetrahedralizations and provably good boundary recovery. In *Eleventh International Meshing Roundtable*, 193–204 (2002).
72. Si, H. TetGen, a Delaunay-based quality tetrahedral mesh generator. *ACM Trans. Math. Softw.* **41**, 11:1–11:36, <https://doi.org/10.1145/2629697> (2015).
73. Rajan, V. T. Optimality of the delaunay triangulation in rd. *Discret. & computational geometry* **12**, 189–202, <https://doi.org/10.1007/BF02574375> (1994).
74. Deuflhard, P. & Weiser, M. *Numerische Mathematik 3 - Adaptive Lösung partieller Differentialgleichungen* (De Gruyter, 2011).
75. Xu, J. & Zikatanov, L. A monotone finite element scheme for convection-diffusion equations. *Math. Comput.* **68**, 1429–1446 (1999).
76. Shewchuk, J. What is a good linear element? Interpolation, conditioning, and quality measures. In *Eleventh International Meshing Roundtable*, 115–126 (2002).
77. Allbritton, N., Meyer, T. & Stryer, L. Range of messenger action of calcium ion and inositol 1, 4, 5-trisphosphate. *Sci.* **258**, 1812–1815, <https://doi.org/10.1126/science.1465619>, <http://www.sciencemag.org/content/258/5089/1812.full.pdf> (1992).
78. Schmidt, H., Stiefel, K. M., Racay, P., Schwaller, B. & Eilers, J. Mutational analysis of dendritic Ca<sup>2+</sup> kinetics in rodent Purkinje cells: role of parvalbumin and calbindin D<sub>28k</sub>. *The J. Physiol.* **551**, 13–32, <https://doi.org/10.1113/jphysiol.2002.035824>, <http://jip.physoc.org/content/551/1/13.full.pdf+html> (2003).
79. Veenstra, T. D., Johnson, K. L., Tomlinson, A. J., Naylor, S. & Kumar, R. Determination of calcium-binding sites in rat brain calbindin D<sub>28k</sub> by electrospray ionization mass spectrometry. *Biochem.* **36**, 3535–3542, <https://doi.org/10.1021/bi9628329> PMID: 9132004 (1997).
80. Nägerl, U. V., Novo, D., Mody, I. & Vergara, J. L. Binding kinetics of calbindin-D<sub>28k</sub> determined by flash photolysis of caged Ca<sup>2+</sup>. *Biophys. J.* **79**, 3009–3018, <http://linkinghub.elsevier.com/retrieve/pii/S0006349500765374>, [https://doi.org/10.1016/S0006-3495\(00\)76537-4](https://doi.org/10.1016/S0006-3495(00)76537-4), <http://www.jbc.org/content/277/19/16662.full.pdf> (2000).
81. Berggård, T. *et al.* Calbindin D<sub>28k</sub> exhibits properties characteristic of a Ca<sup>2+</sup> sensor. *J. Biol. Chem.* **277**, 16662–16672, <https://doi.org/10.1074/jbc.M200415200>, <http://www.jbc.org/content/277/19/16662.full.pdf+html> (2002).
82. Bezprozvanny, I. & Ehrlich, B. E. Inositol (1, 4, 5)-trisphosphate (InsP3)-gated Ca channels from cerebellum: conduction properties for divalent cations and regulation by intraluminal calcium. *The J. Gen. Physiol.* **104**, 821–856, <https://doi.org/10.1085/jgp.104.5.821>, <http://jgp.rupress.org/content/104/5/821.full.pdf+html> (1994).
83. De Young, G. W. & Keizer, J. A single-pool inositol 1, 4, 5-trisphosphate-receptor-based model for agonist-stimulated oscillations in Ca<sup>2+</sup> concentration. *Proc. Natl. Acad. Sci.* **89**, 9895–9899 <http://www.pnas.org/content/89/20/9895.full.pdf+html> (1992).
84. Keizer, J. & Levine, L. Ryanodine receptor adaptation and Ca<sup>2+</sup>-induced Ca<sup>2+</sup> release-dependent Ca<sup>2+</sup> oscillations. *Biophys. J.* **71**, 3477–3487, [https://doi.org/10.1016/S0006-3495\(96\)79543-7](https://doi.org/10.1016/S0006-3495(96)79543-7), <http://download.cell.com/biophysj/pdf/PIIS0006349596795437.pdf> (1996).
85. Tinker, A., Lindsay, A. R. G. & Williams, A. J. Cation conduction in the calcium release channel of the cardiac sarcoplasmic reticulum under physiological and pathophysiological conditions. *Cardiovasc. Res.* **27**, 1820–1825, <https://doi.org/10.1093/cvr/27.10.1820>, <http://cardiovascres.oxfordjournals.org/content/27/10/1820.full.pdf> (1993).
86. Sneyd, J. *et al.* A model of calcium waves in pancreatic and parotid acinar cells. *Biophys. J.* **85**, 1392–1405, <http://www.sciencedirect.com/science/article/pii/S000634950374572X>, [https://doi.org/10.1016/S0006-3495\(03\)74572-X](https://doi.org/10.1016/S0006-3495(03)74572-X) (2003).
87. Graupner, M. A theory of plasma membrane calcium pump function and its consequences for presynaptic calcium dynamics. *Diploma thesis, Technische Universität Dresden* (2003).
88. Nimchinsky, E. A., Yasuda, R., Oertner, T. G. & Svoboda, K. The number of glutamate receptors opened by synaptic stimulation in single hippocampal spines. *J. Neurosci.* **24**, 2054–2064, <https://doi.org/10.1523/JNEUROSCI.5066-03.2004>, <http://www.jneurosci.org/content/24/8/2054.full.pdf> (2004).
89. Jahr, C. E. & Stevens, C. F. Calcium permeability of the N-methyl-D-aspartate receptor channel in hippocampal neurons in culture. *Proc. Natl. Acad. Sci.* **90**, 11573–11577, <https://doi.org/10.1073/pnas.90.24.11573>, <http://www.pnas.org/content/90/24/11573.full.pdf> (1993).
90. Jahr, C. & Stevens, C. Voltage dependence of NMDA-activated macroscopic conductances predicted by single-channel kinetics. *J. Neurosci.* **10**, 3178–3182, <https://doi.org/10.1523/JNEUROSCI.10-09-03178.1990>, <http://www.jneurosci.org/content/10/9/3178.full.pdf> (1990).
91. Saris, N.-E. L., Mervaala, E., Karppanen, H., Khawaja, J. A. & Lewenstam, A. Magnesium: An update on physiological, clinical and analytical aspects. *Clin. Chimica Acta* **294**, 1–26, <http://www.sciencedirect.com/science/article/pii/S0009898199002582>, [https://doi.org/10.1016/S0009-8981\(99\)00258-2](https://doi.org/10.1016/S0009-8981(99)00258-2) (2000).
92. Fink, C. C. *et al.* An image-based model of calcium waves in differentiated neuroblastoma cells. *Biophys. J.* **79**, 163–183, <http://www.sciencedirect.com/science/article/pii/S0006349500762813>, [https://doi.org/10.1016/S0006-3495\(00\)76281-3](https://doi.org/10.1016/S0006-3495(00)76281-3) (2000).
93. van der Vorst, H. A. B-CGSTAB: A fast and smoothly converging variant of Bi-CG for the solution of nonsymmetric linear systems. *SIAM J. on Sci. Stat. Comput.* **13**, 631–644, <https://doi.org/10.1137/0913035>. (1992).
94. Jülich Supercomputing Centre. JURECA: General-purpose supercomputer at Jülich Supercomputing Centre. *J. large-scale research facilities* **2**, <https://doi.org/10.17815/jlsrf-2-121> (2016).

95. Luzzi, V., Sims, C. E., Soughayer, J. S. & Allbritton, N. L. The physiologic concentration of inositol 1, 4, 5-trisphosphate in the oocytes of *Xenopus laevis*. *J. Biol. Chem.* **273**, 28657–28662, <https://doi.org/10.1074/jbc.273.44.28657>, <http://www.jbc.org/content/273/44/28657.full.pdf+html> (1998).
96. Müller, A. *et al.* Endogenous  $\text{Ca}^{2+}$  buffer concentration and  $\text{Ca}^{2+}$  microdomains in hippocampal neurons. *The J. Neurosci.* **25**, 558–565, <https://doi.org/10.1523/JNEUROSCI.3799-04.2005>, <http://www.jneurosci.org/content/25/3/558.full.pdf+html> (2005).
97. Wang, S. S., Alousi, A. A. & Thompson, S. H. The lifetime of inositol 1, 4, 5-trisphosphate in single cells. *The J. Gen. Physiol.* **105**, 149–171, <https://doi.org/10.1085/jgp.105.1.149>, <http://jgp.rupress.org/content/105/1/149.full.pdf+html> (1995).
98. Means, S. *et al.* Reaction diffusion modeling of calcium dynamics with realistic ER geometry. *Biophys. J.* **91**, 537–557, <http://linkinghub.elsevier.com/retrieve/pii/S0006349506717532> (2006).
99. Chiu, V. C. K. & Haynes, D. H. Rapid kinetic studies of active  $\text{Ca}^{2+}$  transport in sarcoplasmic reticulum. *J. Membr. Biol.* **56**, 219–239, <https://doi.org/10.1007/BF01869478> (1980).
100. Elwess, N. L., Filoteo, A. G., Enyedi, A. & Penniston, J. T. Plasma membrane  $\text{Ca}^{2+}$  pump isoforms 2a and 2b are unusually responsive to calmodulin and  $\text{Ca}^{2+}$ . *J. Biol. Chem.* **272**, 17981–17986, <https://doi.org/10.1074/jbc.272.29.17981>, <http://www.jbc.org/content/272/29/17981.full.pdf+html> (1997).

## Acknowledgements

The authors gratefully acknowledge the computing time granted by the John von Neumann Institute for Computing (NIC) and provided on the supercomputer JURECA at Jülich Supercomputing Centre (JSC). This work was supported by Deutsche Forschungsgemeinschaft (CRC974 to AV), BMBF (Collaborative Research in Computational Neuroscience 01GQ1410B to GQ), and a joint NIH/BMBF Collaborative Research Grant to AV and GQ (R01MH118930-01).

## Author Contributions

The study was conceived and supervised by A.V. and G.Q. The model was developed by M.B. and G.Q. Simulations were carried out by M.B. and M.K. M.K. and M.S. developed the spine generator. The manuscript was written by A.V. and G.Q. with the help of M.B. and M.S. A.V., G.Q. and M.B. were involved in data interpretation and critically revising the manuscript.

## Additional Information

**Supplementary information** accompanies this paper at <https://doi.org/10.1038/s41598-018-33343-9>.

**Competing Interests:** The authors declare no competing interests.

**Publisher's note:** Springer Nature remains neutral with regard to jurisdictional claims in published maps and institutional affiliations.



**Open Access** This article is licensed under a Creative Commons Attribution 4.0 International License, which permits use, sharing, adaptation, distribution and reproduction in any medium or format, as long as you give appropriate credit to the original author(s) and the source, provide a link to the Creative Commons license, and indicate if changes were made. The images or other third party material in this article are included in the article's Creative Commons license, unless indicated otherwise in a credit line to the material. If material is not included in the article's Creative Commons license and your intended use is not permitted by statutory regulation or exceeds the permitted use, you will need to obtain permission directly from the copyright holder. To view a copy of this license, visit <http://creativecommons.org/licenses/by/4.0/>.

© The Author(s) 2018